

# Enhanced piezo-photocatalytic water splitting activity via engineering robust dipole moments in covalent organic frameworks

Received: 3 May 2025

Accepted: 2 December 2025

Published online: 12 December 2025

Check for updates

Zi-Zhan Liang<sup>1</sup>, Yixuan Wang<sup>2</sup>, Xin-Ao Li<sup>1</sup>, Xin-Bang Peng<sup>1</sup>, Li Gong<sup>3</sup>, Li-Min Xiao<sup>4</sup>, Xinyi Yang<sup>2</sup>✉, Bo Zou<sup>2</sup>, Yecheng Zhou<sup>1</sup>✉ & Jun-Min Liu<sup>1</sup>✉

Covalent organic frameworks with tunable optical bandgaps and notable piezoelectricity enable sustainable piezo-photocatalytic production of H<sub>2</sub> and H<sub>2</sub>O<sub>2</sub> via pure water splitting. Strong dipole moments can significantly boost piezoelectric properties, necessitating a systematic exploration of their structure-property relationships. Here, we synthesize a series of  $\beta$ -ketoenamine/imine-linked covalent organic frameworks, such as TP-BT-OF/1F/2F-COF, BTA-BT-OF-COF, and TP-SB-COF, through molecular design engineering. The combination of symmetry-breaking benzothiadiazole units and in-plane polarized  $\beta$ -ketoenamine linkages creates a robust dipole moment in TP-BT-OF-COF. This material demonstrates a high piezoelectric coefficient and bandgap narrowing, achieving H<sub>2</sub> and H<sub>2</sub>O<sub>2</sub> production rates of 1501.4 and 1435.8  $\mu\text{mol g}^{-1} \text{h}^{-1}$  under co-exposure to ultrasound (60 W, 40 kHz) and visible light. Density functional theory identifies N<sup>8</sup> and C<sup>6</sup> sites on benzothiadiazole units as potential catalytic sites for H<sub>2</sub> and H<sub>2</sub>O<sub>2</sub> evolution, respectively. Molecular design of covalent organic frameworks with prominent dipole moments advances mechano-optical energy conversion technologies.

Efficient water splitting to produce H<sub>2</sub> and H<sub>2</sub>O<sub>2</sub> is considered a green technology for converting renewable energy into other energy forms<sup>1</sup>. However, the photocatalytic water splitting reactions used for H<sub>2</sub> production typically require sacrificial agents and/or cocatalysts<sup>2–4</sup>. Piezoelectric catalysis through the conversion of mechanical to chemical energy is a promising, environmentally friendly approach to the production of H<sub>2</sub> and H<sub>2</sub>O<sub>2</sub><sup>5,6</sup>. In non-centrosymmetric crystalline materials, mechanical stress in piezoelectric catalysis generates polarized charges and built-in electric fields, driving charge carrier separation and inhibiting recombination<sup>7,8</sup>. Moreover, the piezoelectric-induced polarization

potential drives band bending, promoting electron-hole separation, overcoming the thermodynamic barrier of water oxidation, and thus synergistically boosting catalytic efficiency<sup>9</sup>. A variety of piezoelectric materials, including BiFeO<sub>3</sub>, BaTiO<sub>3</sub>, and g-C<sub>3</sub>N<sub>4</sub>, have been utilized for water splitting to produce H<sub>2</sub> and H<sub>2</sub>O<sub>2</sub> via piezoelectricity<sup>10–14</sup>. However, classical inorganic piezoelectric materials are limited by poor structural tunability and complex polarization processes, which severely hamper their mechanically driven catalytic efficiency<sup>15</sup>. Consequently, the intrinsic structural tunability of framework materials establishes them as highly suitable candidates for emerging piezo-photocatalytic systems<sup>16–19</sup>.

<sup>1</sup>The Key Laboratory of Low-Carbon Chemistry & Energy Conservation of Guangdong Province, School of Materials Science and Engineering, Sun Yat-sen University, Guangzhou, China. <sup>2</sup>State Key Laboratory of Superhard Materials, Synergetic Extreme Condition High-Pressure Science Center, College of Physics, Jilin University, Changchun, China. <sup>3</sup>Instrumental Analysis Research Center, Sun Yat-sen University, Guangzhou, China. <sup>4</sup>School of Computer Science and Engineering, Beihang University, Beijing, China. ✉e-mail: [yangxinyi@jlu.edu.cn](mailto:yangxinyi@jlu.edu.cn); [zhouych29@mail.sysu.edu.cn](mailto:zhouych29@mail.sysu.edu.cn); [liujunm@mail.sysu.edu.cn](mailto:liujunm@mail.sysu.edu.cn)

Covalent organic frameworks (COFs) have emerged as a paradigm-shifting photocatalytic platform. Their ordered nanoporosity and atomically precise structural programmability, achieved through modular covalent assembly, demonstrate their potential as pivotal visible-light-responsive photocatalysts<sup>20–22</sup>. Capitalizing on these programmable attributes, recent advances have exploited this design versatility to create two-dimensional (2D) COFs with engineered non-centrosymmetric frameworks, where symmetry-breaking polarization motifs synergistically enhance piezoelectric responses, thus expanding the scope of piezoelectric research<sup>23,24</sup>. For example, recent work engineered twistable bicarbazole motifs or fluorinated alkyl chains into COFs, enhancing piezoelectric performance<sup>25,26</sup>. Our prior work first reported that a highly crystalline  $\beta$ -ketoenamine-linked COF (EA-COF) could exhibit efficient piezo-photocatalytic  $\text{H}_2$  and  $\text{H}_2\text{O}_2$  production in pure water without any co-catalyst. The piezoelectric properties of EA-COF were mainly attributed to the in-plane polarization of the  $\beta$ -ketoenamine groups within the framework<sup>27</sup>. At present, the structure-performance relationships dictating piezoelectricity in COFs are poorly understood. Thus, deliberate architectural tuning of piezo-photocatalytically tailored COFs requires systematic study to unravel critical design principles.

In this study, we rationally design and synthesize a series of  $\beta$ -ketoenamine/imine-linked BT-COFs exhibiting high piezo-photocatalytic activity through meticulous molecular engineering. The two critical factors governing the performance, such as in-plane polarization units and dipole moment, are systematically explored (Fig. 1).  $\beta$ -Ketoenamine-linked COFs exhibit piezoelectricity from ketoenamine unit in-plane polarization, whereas imine-linked COFs lacking these units have lower performance (Fig. 1A). Adjusting the dipole moment by introducing fluorine atoms or changing the structural unit affects the piezo-photocatalytic performance (Fig. 1B). Among them, TP-BT-0F-COF exhibits the highest piezo-photocatalytic water splitting efficiency, producing  $\text{H}_2/\text{H}_2\text{O}_2$  at rates of 1501.4/1435.8  $\mu\text{mol g}^{-1} \text{h}^{-1}$  under ultrasound (60 W, 40 kHz) and visible light

irradiation, respectively, and also shows good stability with  $\text{H}_2/\text{H}_2\text{O}_2$  production amounts of 18.9/14.5  $\text{mmol g}^{-1}$  within 24 h. The enhanced performance arises from the synergy between ultrasound-induced polarized electric fields and the donor-acceptor benzothiadiazole (BT) unit design, which breaks symmetry to yield strong local dipole polarization. The N<sup>8</sup> and C<sup>6</sup> positions of the BT unit are also confirmed as the potential sites of  $\text{H}_2$  and  $\text{H}_2\text{O}_2$  production by theoretical calculations, respectively. Experimental and computational analyses reveal that the BT-driven charge polarization mechanism enhances both photocatalytic efficiency and piezoelectric response, establishing a robust structure-property relationship for improved piezo-photocatalysis.

## Results

### Synthesis and characterization of $\beta$ -ketoenamine/imine-linked COFs

To facilitate the synthesis of  $\beta$ -ketoenamine-linked isorecticular COFs, 4,4'-diamino-substituted p-terphenyl (SB), 4,4'-(benzo-2,1,3-thiadiazole-4,7-diyl)dianiline (BT-0F), 4,4'-(5-difluorobenzo[c][1,2,5]thiadiazole-4,7-diyl)dianiline (BT-1F) (Figs. S1 and S2) and 4,4'-(5,6-difluorobenzo[c][1,2,5]thiadiazole-4,7-diyl)dianiline (BT-2F)<sup>28</sup> were employed as linking agents and subsequently reacted individually with 1,3,5-triformylphloroglucinol (TP) (Fig. 1C), yielding crystalline TP-SB-COF, TP-BT-0F-COF, TP-BT-1F-COF, and TP-BT-2F-COF. Additionally, upon replacing TP with 1,3,5-benzenetricarboxaldehyde (BTA), the imine-linked BTA-BT-0F-COF bearing the BT-0F ligand was synthesized.

The powder X-ray diffraction (PXRD) results showed a high crystallinity of the synthesized TP-BT-0F-COF (Fig. 2A), BTA-BT-0F-COF (Fig. S3), BT-1F-COF (Fig. S4), TP-BT-2F-COF (Fig. S5) and TP-SB-COF (Fig. S6), respectively, which was in good agreement ( $R_p$  and  $R_{wp} < 10\%$ ) with the Pawley refinement results in space group  $P-6$  (Table S1),  $P-6$  (Table S2),  $P3$  (Table S3),  $P3$  (Table S4), and  $P-3$  (Table S5), respectively, and stacking mode AA. The chemical

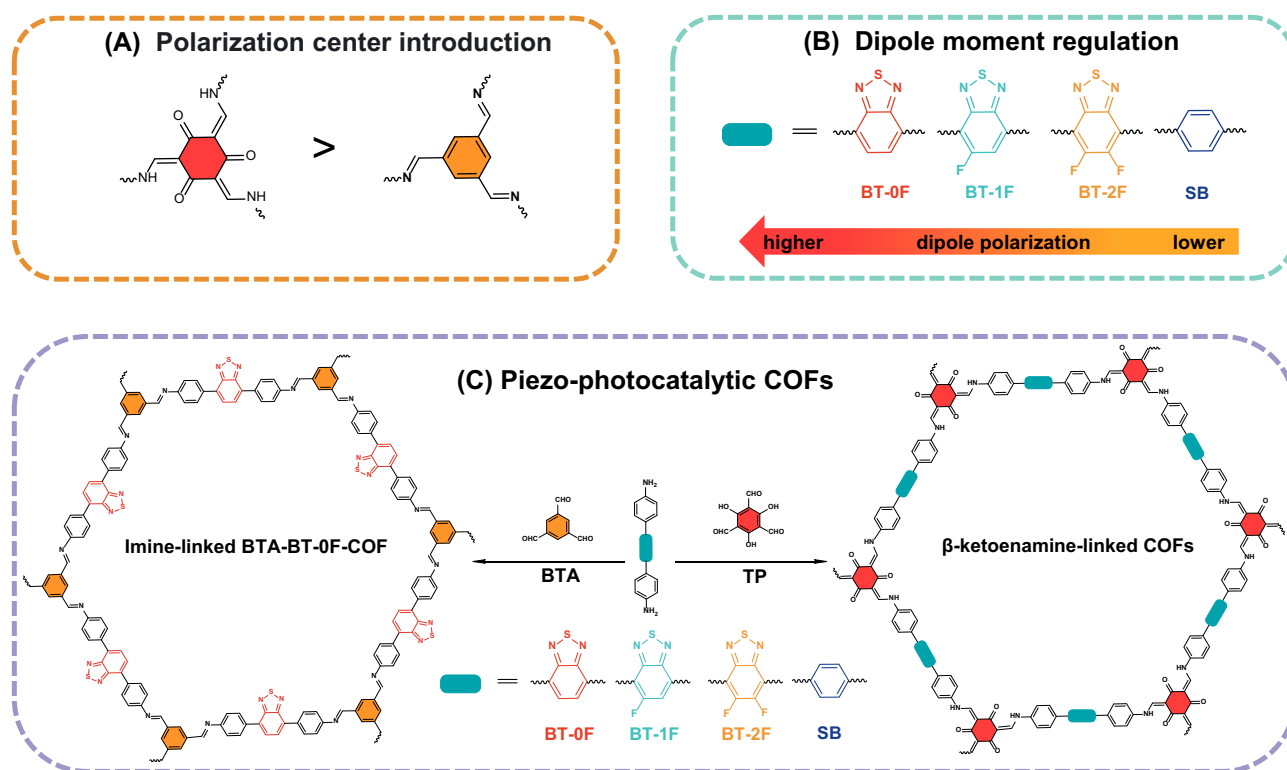


**Fig. 1 | Design of piezo-photocatalytic COFs for water splitting.** COF design strategies of (A) polarization center incorporation and (B) dipole moment optimization; (C) synthesis of  $\beta$ -ketoenamine- and imine-linked COFs.

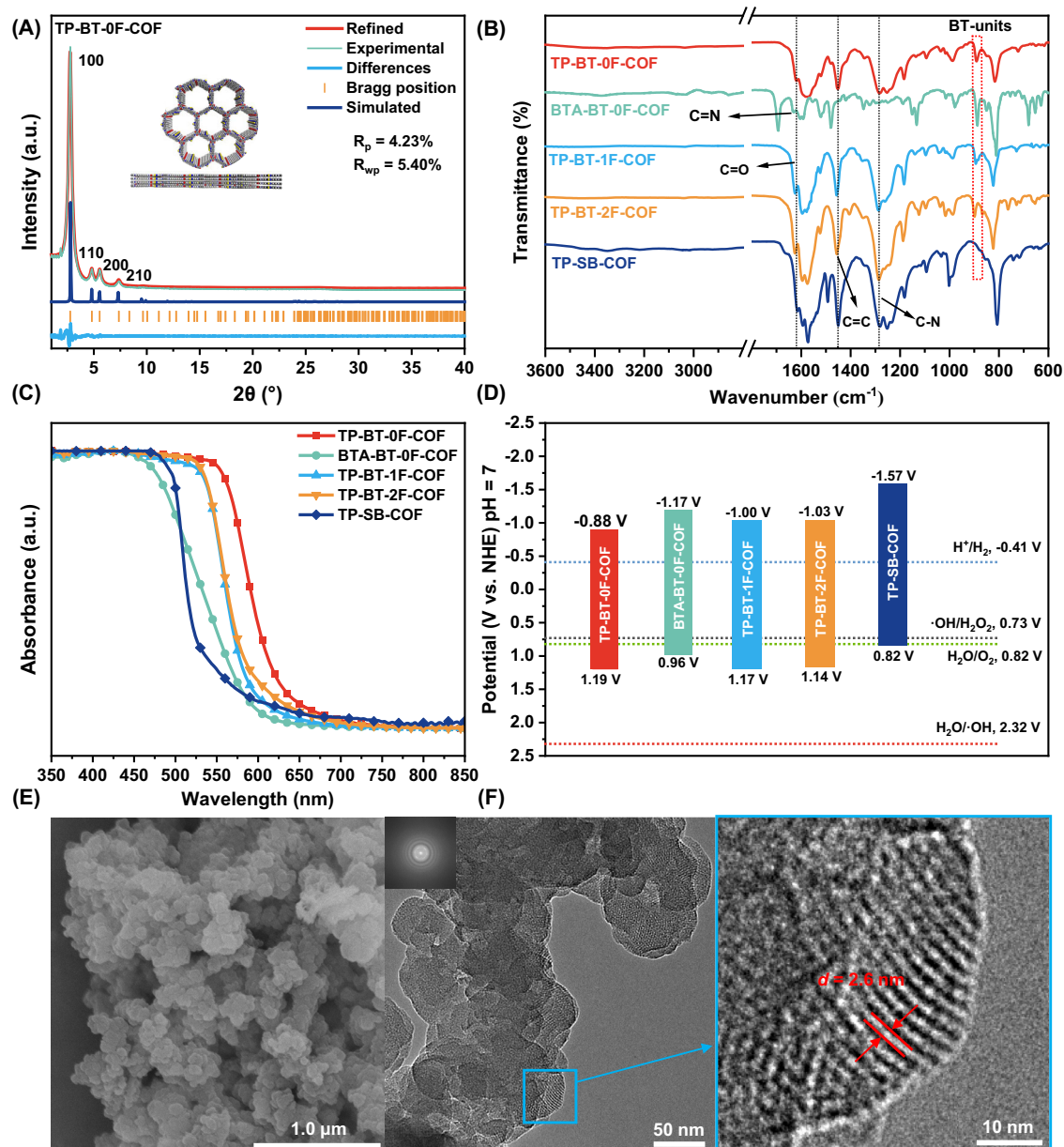


**Fig. 2 | Material characterization of COFs.** **A** Experimental, Pawley-refined, and simulated PXRD patterns of TP-BT-0F-COF, with insets of the ideal eclipsed structure (top and side views,  $R_p$ : unweighted-profile and  $R_{wp}$ : weighted-profile); **B** FT-IR spectra, with arrows indicating the characteristic bands of the  $\beta$ -ketoenamine and imine linkages and dashed red boxes highlighting the spectral features associated

with the BT moiety, **C** UV-vis diffuse reflectance spectra and **D** schematic energy band structures of TP-BT-0F-COF, BTA-BT-0F-COF, TP-BT-1F-COF, TP-BT-2F-COF, and TP-SB-COF; **E** SEM and **F** HRTEM images of TP-BT-0F-COF. The high-magnification TEM image (an inset in **F**) corresponds to the local region denoted by the blue box.

structures of all the resulting COFs were investigated using various analytical methods.

Fourier transform infrared (FT-IR) spectra revealed that the characteristic vibrational frequencies corresponding to the C=O, C=C, and C-N bonds were observed at 1619, 1451, and 1253  $\text{cm}^{-1}$  for TP-BT-0F-COF, respectively (Figs. 2B and S7). These signals were attributed to the formation of  $\beta$ -ketoenamine subunits. These characteristic peaks were also observed in the other three COFs (TP-BT-1F-COF, TP-BT-2F-COF, and TP-SB-COF), demonstrating the effective synthesis of all four COFs (Figs. 1B and S8–S10). Meanwhile, BTA-BT-0F-COF was synthesized via an imine bond, and the peak at 1630  $\text{cm}^{-1}$  was indicative of the imine bond (C=N) (Figs. 2B and S11). The C=O signals at 1694  $\text{cm}^{-1}$  were observed corresponding to the terminal -CHO group on the surface of BTA-BT-0F-COF<sup>28–30</sup>.

The surface chemical states were elucidated by X-ray photoelectron spectroscopy (XPS). In the high-resolution C 1s region (Fig. S12A), TP-BT-0F-COF exhibited two distinct peaks at 284.8 and 286.0 eV, corresponding to carbon atoms in C=C and C-N bonds. The N 1s spectra (Fig. S12B) showed a single nuclear level peak at 399.8 eV for TP-BT-0F-COF, clearly attributed to pyrrolic nitrogen species (=NH), confirming the  $sp^2$  covalent C-N bond in TP-BT-0F-COF. In addition, typical S 2p signals were detected in TP-BT-0F-COF, depicting the sulfur atoms within the benzothiadiazole unit (Fig. S12C). A similar phenomenon was observed in the other four COFs, namely BTA-BT-0F-COF (Fig. S13), TP-BT-1F-COF (Fig. S14), TP-BT-2F-COF (Fig. S15), and TP-SB-COF (Fig. S16). Unlike TP-BT-0F-COF, a single nuclear level peak at 399.2 eV for BTA-BT-0F-COF was attributed to pyridinic nitrogen species (C=N-C), confirming the  $sp^2$  covalent C=N bond in BTA-BT-0F-COF. No S 2p peaks were

found in TP-SB-COF without the benzothiadiazole group. In addition, the presence of a C–F bond was clearly observed in the structure of TP-BT-1F-COF and TP-BT-2F-COF, as indicated by the characteristic binding energy peak at 687.4 eV in the XPS analysis.

Nitrogen adsorption isotherms were measured at 77 K to assess the surface areas and pore structures of the five COFs. The Brunauer-Emmett-Teller (BET) surface areas of the five COFs were calculated to be 1525.4 m<sup>2</sup>/g (TP-BT-0F-COF) (Fig. S17A), 121.2 m<sup>2</sup>/g (BTA-BT-0F-COF) (Fig. S18A), 2925.2 m<sup>2</sup>/g (TP-BT-1F-COF) (Fig. S19A), 2902.3 m<sup>2</sup>/g (TP-BT-2F-COF) (Fig. S20A), and 312.2 m<sup>2</sup>/g (TP-SB-COF) (Fig. S21A). All COFs exhibited a characteristic type IV adsorption isotherm with H3 or H4 hysteresis, indicating their mesoporous nature. This phenomenon could be attributed to the high crystallinity of the  $\beta$ -ketoenamine-bound COFs, which enhanced the regularity of the pore structure. As a result,  $\beta$ -ketoenamine-linked COFs exhibited a significantly larger specific surface area. In contrast, imine-linked COFs had lower crystallinity, resulting in a reduced specific surface area. This observation suggested that the hydroxyl groups in the triformylphenyl-based building blocks significantly influenced the final accessible surface areas of the COFs. The pore size distributions were predominantly concentrated around a narrow range, with peak maxima around 2.8 nm, as determined by the non-local density functional theory (NLDFT) method (Figs. S17–S21B).

Prior to the photocatalytic studies, the light-harvesting properties and bandgaps of these COFs were evaluated using UV-vis diffuse reflectance spectra. TP-BT-0F-COF, BTA-BT-0F-COF, TP-BT-1F-COF, TP-BT-2F-COF and TP-SB-COF exhibited comparatively restricted optical absorption with absorption onset at 599, 590, 585, 585, and 519 nm (Fig. 2C) and a direct optical bandgap of 2.07, 2.13, 2.17, 2.17, and 2.39 eV (Fig. 2D), respectively. Among the five COFs, TP-BT-0F-COF exhibited a pronounced redshift of the absorption onset with a smaller optical bandgap due to the conjugated donor-acceptor (D-A) structures where phenylamine acted as the electron donor and benzothiadiazole as the electron acceptor. This indicated that it exhibited a broader absorption spectrum within the visible light range, thereby suggesting the potential for enhanced photocatalytic performance. Mott-Schottky measurements and valence band X-ray photoelectron spectroscopy (VB-XPS) were carried out to determine the electronic band positions of as-prepared TP-BT-0F-COF. The curve obtained showed typical characteristics of an n-type semiconductor, with a corresponding Fermi level ( $E_f$ ) of  $-0.79$  V vs. normal hydrogen electrode (NHE). The VB-XPS results for TP-BT-0F-COF are shown in Fig. S22, where the measured value of 1.98 eV indicated the energy difference between the  $E_f$  level and the valence band (VB) level. Consequently, the VB energy level for TP-BT-0F-COF was determined to be 1.19 V vs. NHE, and its conduction band (CB) energy level was  $-0.88$  V vs. NHE. The CB and VB of the other four COFs, BTA-BT-0F-COF (Fig. S23), TP-BT-1F-COF (Fig. S24), TP-BT-2F-COF (Fig. S25), and TP-SB-COF (Fig. S26) were derived using the same method. The results showed that the VB potentials for BTA-BT-0F-COF, TP-BT-1F-COF, TP-BT-2F-COF, and TP-SB-COF were measured to be 0.96, 1.17, 1.14, and 0.82 V vs. NHE, respectively. Similarly, the CB potentials were calculated to be  $-1.17$ ,  $-1.00$ ,  $-1.03$ , and  $-1.57$  V vs. NHE for BTA-BT-0F-COF, TP-BT-1F-COF, TP-BT-2F-COF, and TP-SB-COF, respectively. The results indicated that the CB and VB positions were suitable for facilitating the H<sub>2</sub> evolution and water oxidation reactions (Fig. 2D).

Scanning electron microscopy (SEM) images of all COFs clearly showed distinct nanosheet morphologies (Figs. 2E and S27–30A), suggesting a homogeneous and well-defined structure. In addition, high-resolution transmission electron microscopy (HRTEM) further verified the high crystallinity and systematically organized mesoporous architecture of TP-BT-0F-COF (Fig. 2F), reinforcing the precise synthesis and structural coherence of the material. Similar TEM images of TP-BT-0F-COF (Fig. S27B, C), TP-BT-1F-COF (Fig. S28B–D), TP-BT-2F-

COF (Fig. S29B–E), TP-SB-COF (Fig. S30B–E) were obtained, confirming their high crystallinity.

The unusual piezoelectric properties of the five COFs were further investigated using piezoresponse force microscopy (PFM)<sup>31</sup>. The piezoelectric hysteresis loop with a change of 180° under  $\pm 5$  V direct current bias electric field showed a clear hysteresis with a local switching behavior of polarization for TP-BT-0F-COF, BTA-BT-0F-COF, TP-BT-1F-COF, and TP-BT-2F-COF. From the amplitude-voltage butterfly loop, TP-BT-0F-COF had the maximum effective piezoelectric coefficient ( $d_{33}$ ) of approximately 0.92 nm/V (Fig. 3A), while the maximum effective  $d_{33}$  coefficients of BTA-BT-0F-COF, TP-BT-1F-COF and TP-BT-2F-COF were 0.56 nm/V (Fig. S31A), 0.43 nm/V (Fig. S31D) and 0.26 nm/V (Fig. S31G) respectively<sup>32,33</sup>. The results unambiguously indicated that the materials' piezoelectric properties followed the sequence: TP-BT-0F-COF > BTA-BT-0F-COF > TP-BT-1F-COF > TP-BT-2F-COF. In addition, a discernible resonance peak around 112–201 kHz signified the voltage-induced piezoelectric vibrations within the COFs (Figs. 3B and S31B, E, H). The amplitude showed a significant linear correlation with the excitation voltage, confirming the linear piezoelectricity of TP-BT-0F-COF (Fig. 3C), BTA-BT-0F-COF (Fig. S31C), TP-BT-1F-COF (Fig. S31F), and TP-BT-2F-COF materials (Fig. S31I). The butterfly-shaped amplitude hysteresis loops and corresponding phase hysteresis loops dependent on the bias voltage indicated that the polarization of these COFs could be switched by an electric field. Moreover, lateral PFM amplitudes and phase images of TP-BT-0F-COF (Fig. S32), BTA-BT-0F-COF (Fig. S33), TP-BT-1F-COF (Fig. S34), and TP-BT-2F-COF (Fig. S35) were also collected. It was noticeable that no such phenomenon was observed on TP-SB-COF (Fig. S36), indicating that TP-SB-COF lacked piezoelectric properties, which was consistent with the performance tests mentioned below. Furthermore, the direct piezoelectric effect of all COFs was determined by quasi-static method. High piezoelectric coefficient  $d_{33}$  was obtained for TP-BT-0F-COF (5.5 pC/N) (Fig. S37A), BTA-BT-0F-COF (5.1 pC/N) (Fig. S37B), TP-BT-1F-COF (4.7 pC/N) (Fig. S37C) and TP-BT-2F-COF (4.1 pC/N) (Fig. S37D), consistent with the results obtained from PFM measurements. Such a switchable nature of the domain structures provided robust evidence for the occurrence of piezoelectricity in TP-BT-0F-COF, BTA-BT-0F-COF, TP-BT-1F-COF, and TP-BT-2F-COF<sup>25</sup>.

The non-centrosymmetric nature of TP-BT-0F-COF, critical for its piezoelectricity, was also confirmed by second-harmonic generation. Under 1400 nm femtosecond laser irradiation, the COF exhibited a distinct 700 nm second-harmonic signal (Fig. S38A)<sup>34</sup>. Additionally, violation of the mutual exclusion rule was observed, with normally forbidden vibrational peaks (1366, 1189, and 855 cm<sup>-1</sup>) appearing concurrently in IR and Raman spectra (Fig. S38B). This breakdown of selection rules confirmed a non-centrosymmetric lattice.

In situ high-pressure FT-IR spectroscopy was used to further investigate the structural change of TP-BT-0F-COF, BTA-BT-0F-COF, TP-BT-1F-COF, TP-BT-2F-COF, and TP-SB-COF. It revealed systematic blue-shifting of  $\beta$ -ketoenamine C–N/C=C vibrational peaks in TP-BT-0F-COF (Fig. 3D), TP-BT-1F-COF (Fig. S39A), TP-BT-2F-COF (Fig. S39B), and TP-SB-COF (Fig. S39C) under pressure. Quantitatively, at about 15 GPa, TP-BT-0F-COF exhibited maximal shifts (C–N: 1257  $\rightarrow$  1312 cm<sup>-1</sup>,  $\Delta = 55$  cm<sup>-1</sup>, rate = 3.27 cm<sup>-1</sup> GPa<sup>-1</sup>; C=C: 1458  $\rightarrow$  1506 cm<sup>-1</sup>,  $\Delta = 48$  cm<sup>-1</sup>, rate = 3.52 cm<sup>-1</sup> GPa<sup>-1</sup>; Fig. 3E), surpassing fluorinated analogs TP-BT-1F (3.12/3.24 cm<sup>-1</sup> GPa<sup>-1</sup>; Fig. S39D), TP-BT-2F (2.89/2.99 cm<sup>-1</sup> GPa<sup>-1</sup>; Fig. S39E), and non-ketoenamine TP-SB-COF (1.01/1.87 cm<sup>-1</sup> GPa<sup>-1</sup>; Fig. S39F). These blue shifts indicated bond shortening and elevated vibrational frequencies, evidencing pressure-induced dipole moment enhancement within the framework. This intensified structural polarization and intramolecular charge distribution asymmetry<sup>35</sup>. Consequently, TP-BT-0F-COF exhibited the most pronounced shifts, confirming its greater pressure-responsive polarization sensitivity attributable to its inherently larger dipole moment. This directly correlated with the ketoenamine unit being the key structural determinant of COF piezoelectricity.

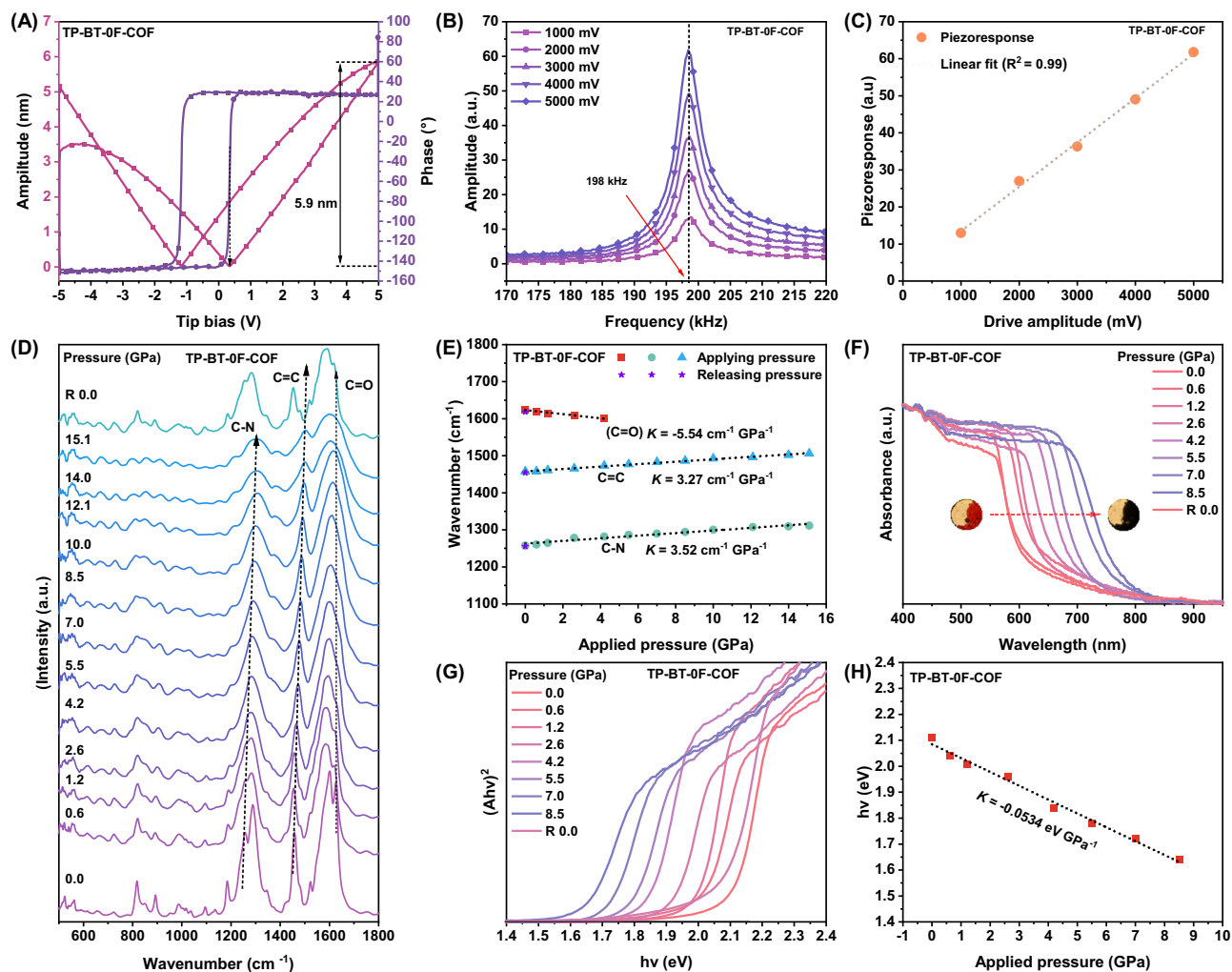


**Fig. 3 | Characterization of piezoelectric properties for TP-BT-0F-COF.** **A** The displacement-voltage and phase curves of TP-BT-0F-COF, showing a maximum amplitude of 5.9 nm; **B** voltage-independent resonance of TP-BT-0F-COF centered near 198 kHz; **C** the linear correlation between the operating voltage and the amplitude of TP-BT-0F-COF; **D** in situ pressure-dependent FT-IR spectroscopy of TP-BT-0F-COF. Key bands indicated by arrows are assigned to C–N, C=C, and C=O

vibrations from the  $\beta$ -ketoenamine units; **E** fitting of the corresponding infrared spectra peaks; **F** in situ pressure-dependent UV-Vis absorption spectroscopy of TP-BT-0F-COF. The insets show optical micrographs of the sample at 0.0 and 8.5 GPa, respectively; **G** corresponding Tauc plots from UV-Vis absorption spectra; **H** corresponding bandgap variation.

Conversely, C=O peaks at  $\sim 1625\text{ cm}^{-1}$  in these samples underwent pressure-induced red-shifting. Most prominently in TP-BT-0F-COF, the  $\beta$ -ketoenamine C=O vibration shifted  $25\text{ cm}^{-1}$  ( $1625 \rightarrow 1600\text{ cm}^{-1}$  at 4.2 GPa) at rate of  $-5.54\text{ cm}^{-1}\text{ GPa}^{-1}$ , significantly exceeding the red-shifting rates of other  $\beta$ -ketoenamine COFs (Fig. S39D–F). This systematic discrepancy quantitatively confirmed that enhanced bond polarization in TP-BT-0F-COF originated from its amplified piezoelectric response, where pressure-driven electron redistribution toward C=C units dispersed C=O electron density<sup>36,37</sup>, reducing bond order and inducing red-shifting.

Concurrently, BTA-BT-0F-COF exhibited pressure-induced blue-shifting of benzene ring vibrations (Fig. S40), attributed to enhanced  $\pi$ -conjugation strengthening C=C bonds. In stark contrast, its imine C=N peak ( $1630\text{ cm}^{-1}$ ) showed negligible shift under pressure, indicating minimal piezoelectric polarization contribution from this linkage. This fundamental disparity in bond responsiveness explained the diminished piezoelectric output of BTA-BT-0F-COF versus  $\beta$ -ketoenamine-based TP-BT-0F-COF, correlating with its inferior catalytic performance.

Density functional theory (DFT) was used to observe and compare the local polarization behavior of the as-synthesized COFs molecules.

As shown schematically in Fig. S41, TP-BT-0F-COF exhibited dipole moments of 1.420 D, which were larger than those of BTA-BT-0F-COF (0.7476 D), TP-BT-1F-COF (0.5995 D), TP-BT-2F-COF (0.4416 D), and TP-SB-COF (0.013 D). By gradually increasing the content of F elements in the skeleton, the dipole moment showed a decreasing tendency. This phenomenon indicated that the introduction of F elements had a significant effect on the charge distribution and molecular polarity of the COF skeleton. During the continuous increase of F elements, the distribution of the electron cloud inside the molecule changed. Due to the relatively strong electronegativity of the F atoms, the electron cloud was more likely to be distributed around the F atoms, thus changing the overall polarity of the molecule and eventually leading to a gradual decrease in the dipole moment. The results indicated that the local dipole moment change was modulated by the introduction of BT derivative units, which enhanced the self-polarization and piezoelectric properties of the COFs. Furthermore, the dipole moment of BTA-BT-0F-COF was lower than that of TP-BT-0F-COF, confirming that  $\beta$ -ketoenamine subunits dominated over BTA motifs in enhancing molecular dipoles and polarization.

Under the current DFT model, our calculations tentatively suggested the presence of piezoelectricity in these COFs. Table S6

presents the calculated ion-clamped piezoelectric tensors of these COFs, which were derived from their response to finite electric fields ( $E = 0.001 \text{ eV/\AA}$ ) under the simulated conditions. The trace of the piezoelectric tensors was 2.626, 1.743, 1.178, and  $-0.351 \text{ e\AA}$  for TP-BT-OF-COF, TP-BT-1F-COF, TP-BT-2F-COF, and TP-SB-COF, respectively, which was in agreement with the *in situ* high-pressure FT-IR spectroscopy results. The origin of piezoelectricity was further investigated. Of all the elements in piezoelectric tensors, the in-plane elements were much larger than the out-plane elements. Tables S6–S10 show the Born effective charges of ions in COFs with charges greater than  $2.0 |e|$  (ion index can be found in Fig. S42), all of which were near the  $\beta$ -ketoenamine group (Fig. S43). As the large piezoelectric elements were mainly in the COF plane, the in-plane norms were calculated to be 4.496, 4.243, 3.341, and  $0.342 \text{ e\AA}$ , respectively. The magnitudes of the trace and the in-plane norms of the tensors were suggestive of a potential correlation with the piezoelectric activities of the COFs. The piezoelectric response of the materials was strongly influenced by their structural components. TP-BT-OF-COF contained both  $\beta$ -ketoenamine and BT units, showing a stronger piezoelectric response due to the active participation of these groups in polarization generation. For BTA-BT-OF-COF, the absence of  $\beta$ -ketoenamine groups reduced the primary piezoelectric active units, resulting in a lower piezoelectric performance. In the case of TP-BT-1F-COF and TP-BT-2F-COF, the introduction of the strong electron-withdrawing fluorine (F) element gradually reduced the skeletal dipole moment, weakened the piezoelectric effect of the BT units, and resulted in similarly low piezoelectric performance. Finally, TP-SB-COF, without BT units, underwent changes in its overall structural symmetry. This altered symmetry was likely the reason for its lack of piezoelectric properties. In conclusion, by tuning the dipole moment of COFs, the polarization effect of COFs could be significantly modulated, thereby tuning their piezoelectric performance.

The piezoelectric potential in piezoelectric materials could generate an intrinsic electric field that modulated charge carrier energy, thereby bending energy bands and enhancing redox activity. *In situ* pressure-dependent UV-visible absorption spectroscopy was used to investigate the redox band positions of COFs, allowing the charge migration process to be monitored. With increasing pressure, the optical absorption spectra of the COF samples showed pronounced red shifts (Figs. S44–S48). TP-BT-OF-COF exhibited maximal bandgap narrowing ( $2.11 \rightarrow 1.64 \text{ eV}$ ,  $\Delta = -0.47 \text{ eV}$ ; rate  $= -0.0534 \text{ eV GPa}^{-1}$ ; Fig. 3F–H), surpassing fluorinated analogs BTA-BT-OF-COF ( $\Delta = -0.40 \text{ eV}$ , rate  $= -0.0496 \text{ eV GPa}^{-1}$ ; Fig. S49A–C), TP-BT-1F-COF ( $\Delta = -0.42 \text{ eV}$ , rate  $= -0.0488 \text{ eV GPa}^{-1}$ ; Fig. S49D–F), and TP-BT-2F-COF ( $\Delta = -0.36 \text{ eV}$ , rate  $= -0.0478 \text{ eV GPa}^{-1}$ ; Fig. S49G–I), and non-ketoenamine TP-SB-COF ( $\Delta = -0.32 \text{ eV}$ , rate  $= -0.0358 \text{ eV GPa}^{-1}$ ; Fig. S49J–L). This bandgap compression enhanced visible-light harvesting and charge migration kinetics, with full reversibility confirmed during decompression (Fig. S50). The distinct response of TP-BT-OF-COF stemmed from its large dipole moment and ketoenamine moieties, which conferred high pressure sensitivity by shifting band positions to reduce electron excitation energy, generating amplified polarized charges under irradiation, and accelerating surface redox processes<sup>38</sup>, collectively enabling an enhanced piezo-photocatalytic performance.

The pronounced piezoelectricity in TP-BT-OF-COF could be traced to the molecular-level symmetry breaking within its framework. This non-centrosymmetry originated not from large torsional motions but from the synergistic interplay of two structural features: the robust in-plane polarization of the  $\beta$ -ketoenamine linkage and the strong electronic asymmetry of the donor-acceptor BT unit. The BT unit created a permanent local dipole, which was maximized in the non-fluorinated analog (TP-BT-OF-COF) as confirmed by its largest calculated dipole moment ( $1.420 \text{ D}$ ). The locked, planar conformation of the  $\beta$ -ketoenamine bond amplified this effect by facilitating efficient charge separation across the framework plane. This mechanistic

picture was supported by the pronounced pressure-induced blue shifts of the  $\beta$ -ketoenamine C–N and C=C vibrations in TP-BT-OF-COF, indicating a highly polarizable structure, and was directly validated by the experimental observation of second-harmonic generation. Consequently, the integration of the polar BT unit within the  $\beta$ -ketoenamine-linked framework provides a powerful design strategy for breaking symmetry and engineering high piezoelectric responses in COFs.

### Piezo-photocatalytic water splitting

To evaluate the piezo-photocatalytic performance of TP-BT-OF-COF, BTA-BT-OF-COF, TP-BT-1F-COF, TP-BT-2F-COF, and TP-SB-COF for  $\text{H}_2$  and  $\text{H}_2\text{O}_2$  evolution from overall water splitting, the following tests were designed. Several regulated experiments for pure water splitting, including photocatalytic, piezocatalytic, and piezo-photocatalytic methods, were performed under optical irradiation, acoustic oscillation ( $60 \text{ W}$ ,  $40 \text{ kHz}$ ), and simultaneous optical and acoustic co-irradiation. Water and a catalytic agent serve as the primary substances in an inert argon environment, with a circulating coolant regulating the reaction temperature, and without the use of any sacrificial reagents or noble metal co-catalysts.

Under the conditions of pure water and visible light irradiation, all COFs could hardly produce  $\text{H}_2$  and only produced  $\text{H}_2\text{O}_2$ . This may be because the COFs reduced the residual oxygen in the water to  $\text{H}_2\text{O}_2$ , as confirmed by other studies<sup>39,40</sup>. Among the four COFs, TP-BT-2F-COF showed the highest  $\text{H}_2\text{O}_2$  production ( $335.4 \mu\text{mol g}^{-1} \text{ h}^{-1}$ ), followed by TP-BT-OF-COF ( $242.2 \mu\text{mol g}^{-1} \text{ h}^{-1}$ ), while BTA-BT-OF-COF ( $128.0 \mu\text{mol g}^{-1} \text{ h}^{-1}$ ) and TP-SB-COF ( $140.7 \mu\text{mol g}^{-1} \text{ h}^{-1}$ ) showed much lower performance (Fig. S51).

When ultrasonic irradiation was applied,  $\text{H}_2/\text{H}_2\text{O}_2$  production occurred on TP-BT-OF-COF, BTA-BT-OF-COF, TP-BT-1F-COF, and TP-BT-2F-COF. It was noteworthy that the oxidation product of  $\text{H}_2\text{O}$  was value-added  $\text{H}_2\text{O}_2$ , illustrating that the piezo-potential induced positive charge ( $q^+$ ) oxidized  $\text{OH}^-$  to  $\text{H}_2\text{O}_2$  instead of  $\text{O}_2$ . As shown in Fig. 4A, B, the  $\text{H}_2/\text{H}_2\text{O}_2$  evolution rate of TP-BT-OF-COF, BTA-BT-OF-COF, TP-BT-1F-COF, and TP-BT-2F-COF was  $1115.2/1019.1$ ,  $708.1/642.1$ ,  $441.4/398.9$ , and  $130.7/112.9 \mu\text{mol g}^{-1} \text{ h}^{-1}$ , respectively. The time-dependent  $\text{H}_2$  and  $\text{H}_2\text{O}_2$  yields over different samples and control groups showed that TP-SB-COF did not exhibit  $\text{H}_2$  evolution due to its lack of piezoelectric properties, and the sonolysis of water was negligible. Under pure ultrasound conditions, the  $\text{H}_2\text{O}_2$  yield of all samples was slightly lower than that of  $\text{H}_2$ , rather than 1:1. This was mainly due to the fact that not all hydroxyl radicals were fully combined to form  $\text{H}_2\text{O}_2$ .

Subsequently, visible light ( $\lambda \geq 420 \text{ nm}$ ) was introduced into the ultrasound reaction system, which further enhanced  $\text{H}_2$  and  $\text{H}_2\text{O}_2$  evolution for both samples. Under simultaneous irradiation by light and ultrasound, TP-BT-OF-COF exhibited a prominent  $\text{H}_2/\text{H}_2\text{O}_2$  production rate of  $1501.4/1435.8 \mu\text{mol g}^{-1} \text{ h}^{-1}$ , which was competitive among reported COF-based catalysts and other piezocatalysts (Table S11). These values were 1.6/1.6, 2.3/2.5, and 5.9/4.2 times those of BTA-BT-OF-COF ( $938.3/914.4 \mu\text{mol g}^{-1} \text{ h}^{-1}$ ), TP-BT-1F-COF ( $649.8/569.84 \mu\text{mol g}^{-1} \text{ h}^{-1}$ ), and TP-BT-2F-COF ( $250.7/339.7 \mu\text{mol g}^{-1} \text{ h}^{-1}$ ) (Fig. 4C–E). The synergistic contributions of their photo- and piezocatalytic processes were quantified as 26% (photo): 74% (piezo) for TP-BT-OF-COF, 25% (photo): 75% (piezo) for BTA-BT-OF-COF, 32% (photo): 68% (piezo) for TP-BT-1F-COF, and 48% (photo): 52% (piezo) for TP-BT-2F-COF, respectively. The improved piezo-photocatalytic performance suggested the significant role of illumination in promoting the piezocatalytic activity.

The long-term duration experiment of TP-BT-OF-COF was also performed. TP-BT-OF-COF showed good stability with  $\text{H}_2/\text{H}_2\text{O}_2$  production levels of  $18.9/14.5 \text{ mmol/g}$  over 24 h, and its performance in water splitting remained consistent after long piezo-photocatalytic testing (Fig. S52). Although the XRD peak intensities were diminished post-reaction, the nearly unchanged FT-IR spectra confirmed the

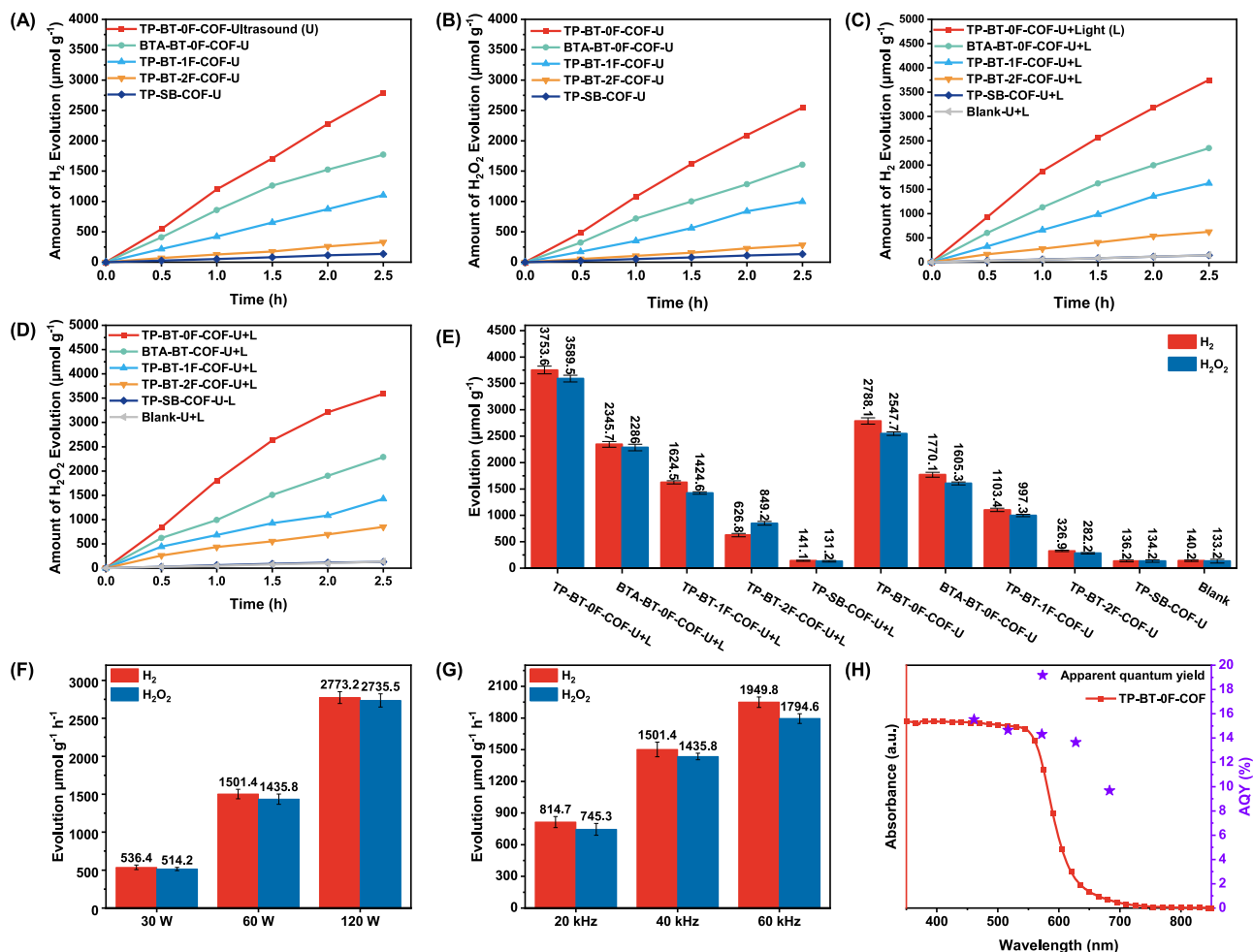


**Fig. 4 | Evaluation of the piezo-photosynthetic H<sub>2</sub> and H<sub>2</sub>O<sub>2</sub> production over a series of COFs.** **A** H<sub>2</sub> and **B** H<sub>2</sub>O<sub>2</sub> yields under ultrasonic irradiation alone; **C** H<sub>2</sub> and **D** H<sub>2</sub>O<sub>2</sub> yields under simultaneous light and ultrasound irradiation; **E** comparison of the total H<sub>2</sub> and H<sub>2</sub>O<sub>2</sub> yields after 2.5 h; **F** H<sub>2</sub> and H<sub>2</sub>O<sub>2</sub> production over TP-BT-OF-COF as a function of ultrasound power at a 40 kHz frequency; **G** H<sub>2</sub> and H<sub>2</sub>O<sub>2</sub> production as a function of ultrasound frequency at a 60 W power; **H** AQYs and

solid-state UV-Vis absorption spectrum of TP-BT-OF-COF. Experimental conditions for (A–E): catalyst (0.1 mg mL<sup>-1</sup>) in 20 mL deionized water, ultrasonic irradiation (40 kHz, 60 W), and visible light ( $\lambda \geq 420$  nm, 1000 W m<sup>-2</sup>), temperature maintained at 20 ± 0.5 °C. Error bars in (E–G) represent the standard deviation from three independent measurements; AQY data in (H) is from a single measurement.

robust structural integrity of the TP-BT-OF-COF framework throughout piezo-photocatalysis (Fig. S53).

Compared to the other COFs, the higher H<sub>2</sub> and H<sub>2</sub>O<sub>2</sub> production of TP-BT-OF-COF could be due to its greater piezoelectricity and more efficient vibration energy harvesting. Interestingly, this phenomenon differed from photocatalysis and was mainly attributed to structural differences between the COFs, which led to variations in their piezoelectric performance. Firstly, TP-SB-COF, which lacked the BT unit, completely lost its piezoelectric performance and showed a low hydrogen evolution rate, comparable to that of pure water under the same conditions. Moreover, the absence of  $\beta$ -ketoenamine groups in BTA-BT-OF-COF and the increase in F elements in TP-BT-1F-COF and TP-BT-2F-COF also resulted in a reduction in piezoelectric performance. In addition, under the combined effects of light irradiation and ultrasound, TP-BT-2F-COF was the only material where H<sub>2</sub>O<sub>2</sub> production exceeded hydrogen evolution. This phenomenon was probably due to the introduction of two F atoms, which could promote the generation of H<sub>2</sub>O<sub>2</sub> originating from the CB of TP-BT-2F-COF<sup>41</sup>.

The piezo-photocatalytic activity of TP-BT-OF-COF was systematically evaluated under ultrasonic powers of 30, 60, and 120 W while keeping all other reaction conditions identical (Fig. 4F). The evolution rates of H<sub>2</sub> and H<sub>2</sub>O<sub>2</sub> increased steadily with rising ultrasonic power,

achieving a pronounced piezo-photocatalytic synergy at 120 W (2773.2 μmol g<sup>-1</sup> h<sup>-1</sup> for H<sub>2</sub> and 2735.5 μmol g<sup>-1</sup> h<sup>-1</sup> for H<sub>2</sub>O<sub>2</sub>). This enhancement stemmed from higher ultrasonic power inducing stronger polarization within TP-BT-OF-COF, which generated more pronounced built-in electric fields that facilitated the separation of photogenerated carriers, thereby boosting catalytic efficiency. In sharp contrast, no discernible H<sub>2</sub> and H<sub>2</sub>O<sub>2</sub> production was detected under milder mechanical perturbations (e.g., 800 rpm stirring, Fig. S54), thereby emphasizing the critical role of ultrasound-driven piezoelectric activation. The following frequency-dependent studies showed a steady rise in H<sub>2</sub> yield with increasing ultrasound frequency, peaking at 60 kHz. This optimal response was likely due to the proximity to the intrinsic resonant frequency of TP-BT-OF-COF, where maximal mechanical energy transfer occurred (Fig. 4G). Wavelength-dependent apparent quantum yield (AQY) measurements were performed on 2 mg of TP-BT-OF-COF using a series of band-pass filters as shown in Fig. 3H. In particular, the AQYs of P-BT-OF-COF were 15.50% (450 nm), 14.61% (500 nm), 14.30% (550 nm), 13.62% (600 nm), and 9.65% (650 nm), respectively. The observed gradual decline in AQYs with increasing wavelength correlated with the optical absorption edge of TP-BT-OF-COF, substantiating the notion that light-driven carrier generation played an essential role.

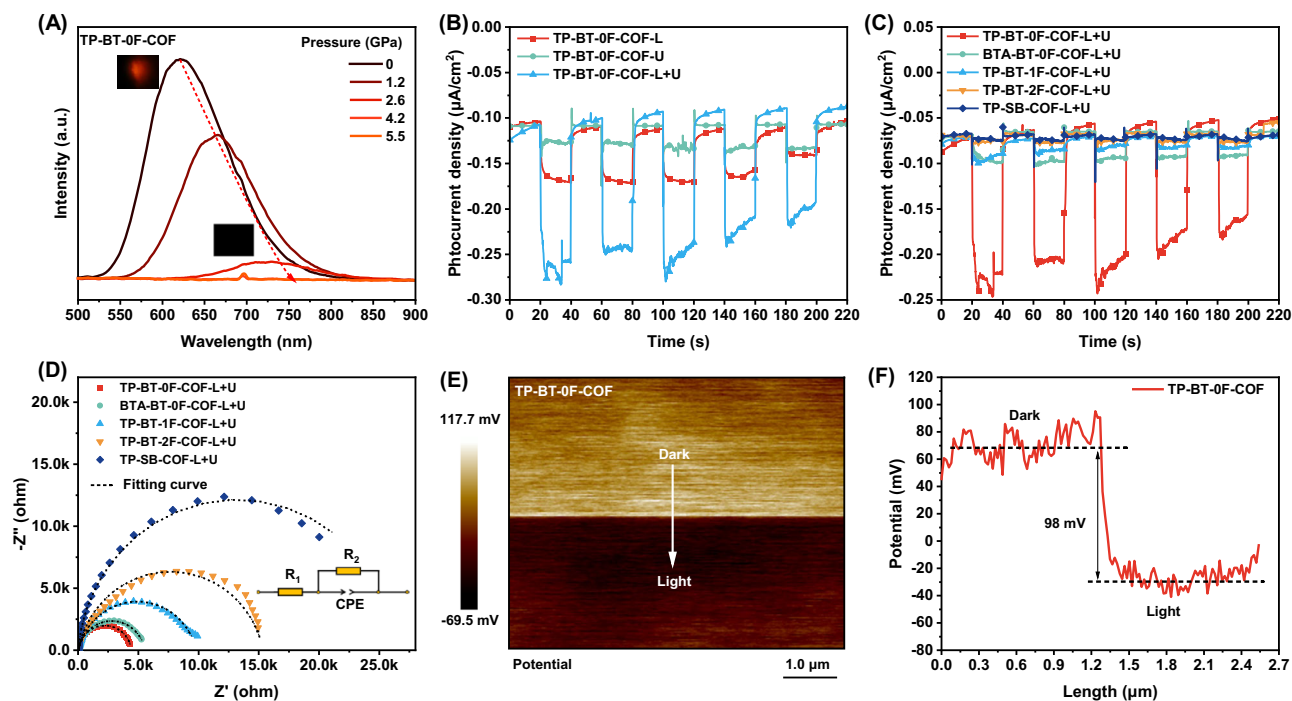


**Fig. 5 | Charge separation dynamics in COFs.** **A** In situ pressure-dependent PL spectra of TP-BT-0F-COF, with insets showing optical micrographs at 0.0 and 5.5 GPa; **B** comparison of PL peak intensities of TP-BT-0F-COF, BTA-BT-0F-COF, TP-BT-1F-COF, and TP-BT-2F-COF under 1.2 GPa; **C** photocurrent responses and **D** EIS Nyquist plots of all COFs measured under visible light and ultrasound ( $R_1$ : series

resistance;  $R_2$ : charge-transfer resistance; CPE: constant phase element); **E** KPFM potential images of TP-BT-0F-COF in the dark and under illumination; **F** the corresponding surface potential difference, indicating a 98 mV shift upon light illumination.

### Mechanism of piezo-photocatalysis

Scavenger-assisted mechanistic studies elucidated the charge transfer pathways in piezo-photocatalysis (Fig. S55). Selective electron depletion with 10 mM  $\text{AgNO}_3$  suppressed  $\text{H}_2$  evolution by 90%, verifying the electron-mediated proton reduction ( $2\text{H}^+ + 2\text{e}^- \rightarrow \text{H}_2$ ,  $-0.41\text{ V vs. NHE}$ ). Concurrently, the 87% decrease in  $\text{H}_2\text{O}_2$  yield upon hole scavenging (10 mM EDTA-2Na) and 91% reduction with hydroxyl radical quenching (10 vol% tert-butanol, TBA) collectively demonstrated that holes drove the indirect two-electron water oxidation pathway ( $\text{H}_2\text{O} + \text{h}^+ \rightarrow \cdot\text{OH} + \text{H}^+$ ,  $2.32\text{ V vs. NHE}$ ;  $2\cdot\text{OH} \rightarrow \text{H}_2\text{O}_2$ ,  $0.74\text{ V vs NHE}$ )<sup>42,43</sup>.

Isotopic labeling experiments using  $\text{D}_2\text{O}$  (95%) in the reduction halves confirmed the origin of the produced  $\text{H}_2$ . The molecular ion peak at  $m/z = 4.00$  in the mass spectrum indicated  $\text{D}_2$  production from  $\text{D}_2\text{O}$  (Fig. S56)<sup>34</sup>. To further investigate the water oxidation reaction (WOR) in piezo-photocatalytic water splitting,  $\cdot\text{OH}$  generation was measured using terephthalic acid photoluminescence (TA-PL) assays<sup>10</sup>. As shown in Fig. S57, the TA-OH fluorescence intensities of all COFs followed the order: TP-BT-0F-COF > BTA-BT-0F-COF > TP-BT-1F-COF > TP-BT-2F-COF > TP-SB-COF, under both ultrasonic irradiation and combined light-ultrasound excitation. This trend aligned with their hierarchical piezo-photocatalytic performance, confirming that  $\cdot\text{OH}$  was a key indicator of WOR efficiency. In contrast, significantly weaker fluorescence occurred under light irradiation alone (Fig. S58), as photogenerated electrons primarily drove the oxygen reduction reaction (ORR) to form  $\cdot\text{OH}$ , rather than direct water oxidation. This was consistent with the VB positions of all COFs being significantly more positive than the thermodynamic potential for the indirect  $2\text{e}^-$  two-step WOR, precluding  $\cdot\text{OH}$  generation via water oxidation under sole photocatalysis. In situ electron paramagnetic resonance (EPR) analysis revealed four characteristic signals of  $\cdot\text{OH}$  radicals for TP-BT-0F-COF under combined ultrasound and light irradiation, with negligible signals observed in light-only controls (Fig. S59). This confirmed the occurrence of an indirect  $2\text{e}^-$  two-step WOR pathway exclusively

under piezo-photocatalytic conditions, and its absence under photocatalytic conditions alone. To further investigate the origin of  $\cdot\text{OH}$ , an isotopic labeling experiment was conducted using  $\text{H}_2^{18}\text{O}$  (98%) as the reaction solution. Benzoic acid served as a  $\cdot\text{OH}$  trap, oxidizing to *p*-hydroxybenzoic acid<sup>44</sup>. The observation of a molecular ion peak at  $m/z = 139.0296$  (Fig. S60) corresponded to the formation of  $^{18}\text{O}$ -labeled *p*-hydroxybenzoic acid, confirming that the  $\cdot\text{OH}$  originated from  $\text{H}_2^{18}\text{O}$ . This result provided direct evidence that  $\text{H}_2\text{O}_2$  originated from water oxidation during piezo-photocatalysis.

In situ pressure-dependent photoluminescence (PL) spectroscopy measurements were conducted to examine the charge recombination dynamics (Fig. 5A). Under increasing pressure (0.0  $\rightarrow$  5.0 GPa), the four COFs initially exhibited a red coloration, which transitioned to a colorless state at higher pressures, as shown in Figs. S61 and S62. Fluorescence quenching occurred for the four COFs at about 2.0 GPa, accompanied by a pronounced redshift with increasing pressure. The emission quenching resulted from the significant enhancement of  $\pi$ - $\pi$  interactions at elevated pressures, leading to a continuous redshift<sup>24,45</sup>. Consequently, 2D COFs with extensive conjugation and densely packed structures were more prone to fluorescence quenching. This implied that charge carriers within the COF separated and transferred at an increased rate under the influence of pressure. Ultimately, this promoted the generation of more electrons and holes and thus increased their accessibility for redox reactions. Notably, TP-BT-0F-COF exhibited the most suppressed PL intensity at equivalent pressures, directly correlating with its high piezo-photocatalytic carrier separation efficiency.

The charge conduction characteristics in the piezo-photocatalytic process were investigated by piezo-electrochemical measurements. The photocurrent-time curves were recorded under visible light, ultrasound, or a combination of both to confirm the charge conduction behavior of TP-BT-0F-COF<sup>46</sup>. TP-BT-0F-COF exhibited higher photocurrent densities when exposed to both ultrasound and light simultaneously compared to light/ultrasound alone, demonstrating

that ultrasound/light enhanced the charge transfer efficiency of the material (Fig. 5B). As shown in Fig. 5C, the transient photocurrents under light and ultrasound exposure were in the order of TP-BT-OF-COF > BTA-BT-OF-COF > TP-BT-IF-COF > TP-BT-2F-COF > TP-SB-COF, consistent with the piezo-photocatalytic results above. TP-BT-OF-COF exhibited the higher photocurrent density compared to the other four COFs, suggesting that charge separation and transfer were more efficient in TP-BT-OF-COF. This improvement in charge transfer allowed a greater number of piezoelectric charges to be used to drive electrochemical reactions during the photopiezoelectric catalytic process.

To further investigate the charge transfer resistance, electrochemical impedance spectroscopy (EIS) measurements of the TP-BT-OF-COF electrodes were performed under different conditions, and the corresponding Nyquist plots and fitting results are shown in Fig. S63B and Table S12. As depicted in the equivalent circuit diagram,  $R_2$  corresponds to the charge transfer resistance at the sample/electrolyte interface, whereas  $R_1$  represents the resistance of the electrolyte and other related system resistances. Notably, when both light and ultrasound were applied simultaneously, the charge transfer resistance was significantly reduced compared to either light or ultrasound alone, suggesting an improved electronic interaction between piezoelectric charges and electroactive materials under these combined conditions<sup>47</sup>. In addition, the semicircular radius of the EIS Nyquist plots and  $R_2$  of the five COFs decreased in the order of TP-BT-OF-COF (4392  $\Omega$ ) < BTA-BT-OF-COF (5513  $\Omega$ ) < TP-BT-IF-COF (9767  $\Omega$ ) < TP-BT-2F-COF (15,310  $\Omega$ ) < TP-SB-COF (26,326  $\Omega$ ) (Fig. 5D, Table S13), indicating that the solid-phase interfacial resistance and surface charge transfer barrier were lower in TP-BT-OF-COF compared to the other materials.

The surface potentials of the COFs were measured both in the dark and under irradiation using Kelvin probe force microscopy (KPFM). As shown in Fig. 5E, F, TP-BT-OF-COF exhibited a surface potential of 68 mV in the dark, which decreased to -30 mV upon exposure to light. The observed decrease of 98 mV was probably due to the effect of the inward piezoelectric potential field<sup>48,49</sup>. The similar trend was also observed for the other three COFs, but their potential differences of 58 mV for BTA-BT-OF-COF (Fig. S64A, B), 80 mV for TP-BT-IF-COF (Fig. S64C, D), and 76 mV for TP-BT-2F-COF (Fig. S64E, F) were all lower than that of TP-BT-OF-COF. These results could be attributed to the piezo-induced polarization charge being partially depleted by photogenerated carriers, which was beneficial for the separation of photogenerated charges and improvement of catalytic activity<sup>11,32</sup>.

To reveal the overall water splitting processes, DFT calculations were then performed to reveal possible reactions such as the hydrogen (HER), oxygen (OER), and H<sub>2</sub>O<sub>2</sub> evolution reactions in the piezo-photocatalytic reactions. Normally, HER occurs at the cathode, which provides electrons for the H<sup>+</sup> to form H<sub>2</sub>. Therefore, the reaction active site should be close to the region where the conduction band is distributed. For the same reason, the active site of the OER should be close to the valence band region. Figure 6A, B shows the orbitals of the conduction band minimum and the valence band maximum of TP-BT-OF-COF, and the corresponding band structures are shown in Fig. S65. For the HER, the possible active sites were indexed by the number of O<sup>1</sup>, N<sup>2</sup>, C<sup>3</sup>, C<sup>4</sup>, C<sup>5</sup>, N<sup>6</sup> and S<sup>9</sup> (Fig. 6C), and the calculated corresponding free energy penalties for H<sup>+</sup> adsorption on these sites are shown in Fig. 6D. In general, the N ion in the BT unit (site N<sup>6</sup>) has the lowest free energy requirement of 0.65 eV.

For OERs and H<sub>2</sub>O<sub>2</sub> evolution reactions, the reaction path became very complicated due to multiple steps and reaction intermediates. Finding reaction paths on very large unit cells, such as COFs, was computation-consuming. Therefore, a reasonable simplified model was required, such as the simplified molecular model<sup>28</sup>. Here, we simplified the linking unit by a double carbon bond and obtained a one-dimensional chain (Fig. S66A), and then tested the free energy changes of the HER compared to the original model (Figs. 6D and S66B). It was found that the energy errors near the linker (sites N<sup>2</sup>, C<sup>3</sup>, and C<sup>4</sup>)

were higher by 0.2 eV. It became minimal for the sites on the BT unit (site C<sup>6</sup>, N<sup>6</sup>, and S<sup>9</sup>) where the OER occurred according to the orbital distribution of the VB maximum. Therefore, the simplified model was used to search for OER paths for acceleration. The error of this model should be less than 0.1 eV. Figures 6E and S67 show the possible OER pathways of TP-BT-OF-COF starting from C<sup>6</sup>. The first step was OH<sup>-</sup> adsorption, which was found to be the most difficult step. The free energy required was 2.14 eV, resulting in an overpotential of 0.91 eV. The OER could also start by adsorbing OH<sup>-</sup> on the S<sup>9</sup> and N<sup>6</sup> sites of the BT unit (Fig. 6F). For example, when OH<sup>-</sup> was adsorbed on the S<sup>9</sup> ion, the free energy increase was 2.29 eV, which was 0.15 eV higher than when adsorbed on the C<sup>6</sup> ion. The adsorption on the N<sup>6</sup> ion was much higher, which was unlikely to occur. We focused here on the reactions starting from the C<sup>6</sup> ion. After an OH<sup>-</sup> adsorption, there were four possible subsequent reaction pathways (Fig. S67). Path 1: The transfer of an H to the neighboring C<sup>5</sup> site led to a decrease in energy. However, the next reaction step of adsorbing another OH<sup>-</sup> required an incoming energy of 1.66 eV, followed by the removal of the H and release of an O<sub>2</sub> with energy increases of 1.15 and 0.82 eV, respectively. Path 2: Removing an H from the adsorbed OH<sup>-</sup> increased the energy by about 0.56 eV. The free energy increase for the next OH<sup>-</sup> adsorption was 1.46 eV. Removing O had an energy increase of 1.17 eV. The final step of releasing O<sub>2</sub> would occur spontaneously with an energy decrease of 0.41 eV. Path 3: Adsorption of another OH<sup>-</sup> had to absorb 0.63 eV. The coupling of two OH<sup>-</sup> would produce H<sub>2</sub>O<sub>2</sub>, costing only 0.68 eV. Path 4: Same as pathway 3, adsorption of another OH<sup>-</sup> would have to absorb 0.63 eV, then continuous removal of Hs from the two adsorbed OH<sup>-</sup>s would release O<sub>2</sub> with a maximum energy penalty of 1.39 eV. The possible OERs were fully investigated on other sites and are shown in Fig. S68. It was found that OERs on COF were not able to form the \*O-OH bond (\* is for the adsorption site), which was the rate-determining step for most OERs catalyzed by inorganic catalysts<sup>50</sup>. The O-O bond in COF-catalyzed OERs was formed by the linkage of \*O-O\*. The most favorable reaction path for O<sub>2</sub> production after initial OH<sup>-</sup> adsorption required a minimum energy cost of 1.39 eV, which was twice that for H<sub>2</sub>O<sub>2</sub> production.

Based on the current DFT-derived insights and simulated conditions, OERs appeared to be inactive in this piezo-photocatalytic system, while the H<sub>2</sub>O<sub>2</sub> evolution reactions might preferentially follow pathway 3. This pathway started with an OH<sup>-</sup> absorption at the C<sup>6</sup> ion site with an energy cost of 2.14 eV, and continued with two low-energy cost steps of further OH<sup>-</sup> adsorption and H<sub>2</sub>O<sub>2</sub> release. Combining the experimental and DFT calculation results, we proposed a possible mechanism for piezo-photocatalytic water splitting using TP-BT-OF-COF as an example (Fig. 6G). Upon visible light and ultrasound stimulation, TP-BT-OF-COF underwent deformation and bending, inducing in-plane stretching and compression. The mechanical strain changed the state of the local dipoles, inducing spontaneous polarization and generating a variable piezoelectric field that modulated the energy band structure of TP-BT-OF-COF. As a result, the free electrons in N<sup>6</sup> site of the BT unit were captured by adsorbed H<sup>+</sup> to produce H<sub>2</sub>, while holes were consumed by adsorbed OH<sup>-</sup> and H<sub>2</sub>O at C<sup>6</sup> site of the BT unit to produce oxidation products such as \*OH and H<sub>2</sub>O<sub>2</sub>, thereby facilitating the water splitting reaction.

## Discussion

In summary, we have designed and synthesized a series of BT-functionalized 2D COFs (TP-BT-OF/IF/2F-COF and BTA-BT-OF-COF) with engineered asymmetry, polarity, and dipole polarization to enable piezoelectricity. Piezoelectric properties were verified through PFM and piezoelectric coefficient measurements. Pressure-dependent in situ FT-IR, PL, and UV-vis spectroscopy elucidated the water-splitting mechanism, while DFT calculations identified the N<sup>6</sup> and C<sup>6</sup> sites on the BT unit as potential active centers for H<sub>2</sub>/H<sub>2</sub>O<sub>2</sub> production. TP-BT-OF-COF demonstrated optimal piezo-photocatalytic performance, achieving H<sub>2</sub>/H<sub>2</sub>O<sub>2</sub> production rates of 1501.4/1435.8  $\mu\text{mol g}^{-1} \text{h}^{-1}$  and sustained stability (18.9/14.5 mmol g<sup>-1</sup> over 24 h) under ultrasound (60 W, 40 kHz)

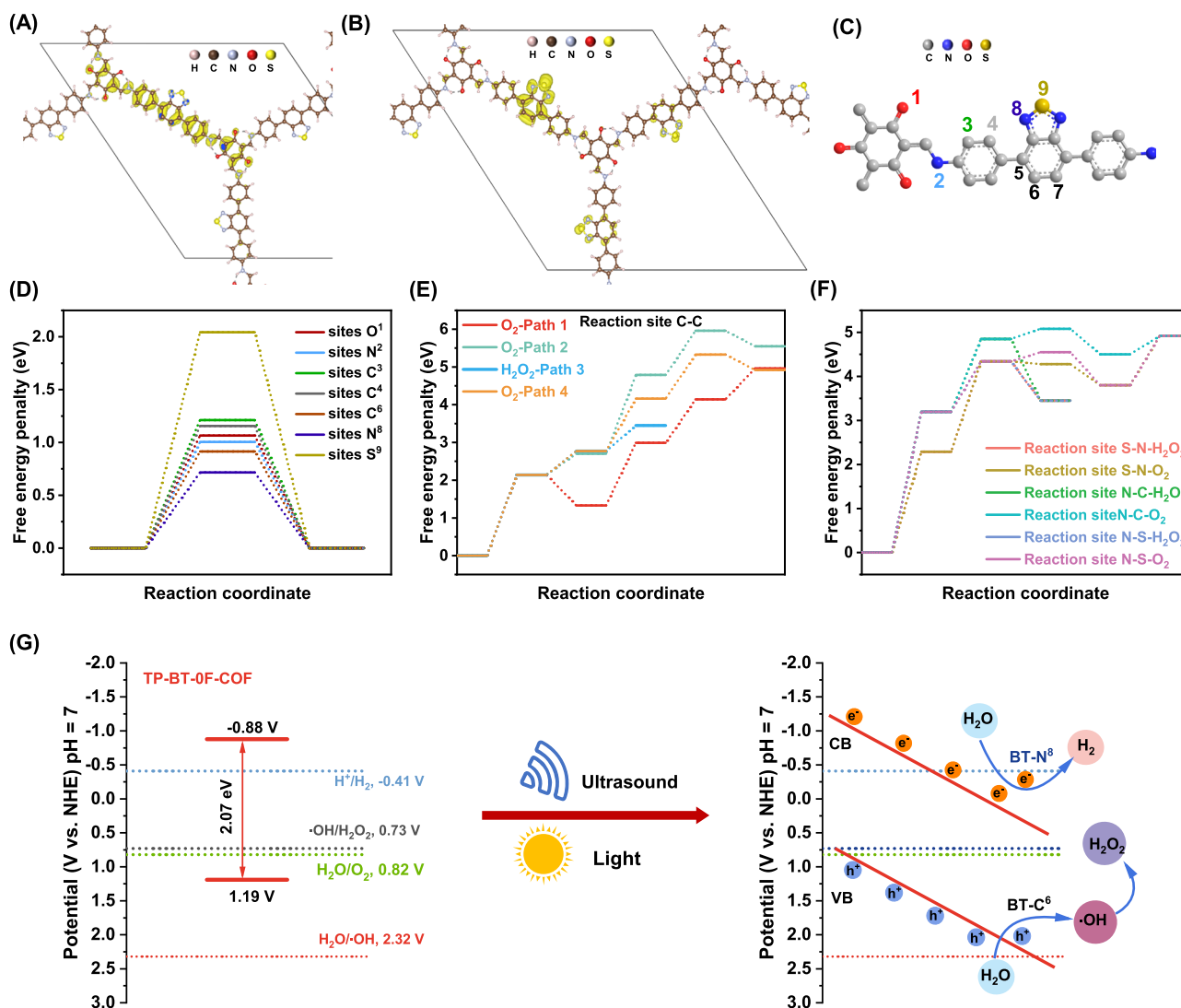


**Fig. 6 | DFT calculation and mechanism study.** The electron density distributions at the (A) CB minimum and B VB maximum; C the possible active sites of HER; D the free energy penalties on active sites; E the free energy of OER at the C–C site and the

possible subsequent reaction pathways of OER; F the free energy of OER at the S–N, N–S, and N–C sites; G the schematic diagram of the mechanism for water splitting over TP-BT-OF-COF under piezo-photocatalysis.

and visible light irradiation. The inferior piezoelectric-photocatalytic performance of BTA-BT-OF-COF, TP-BT-1F/2F-COF, and TP-SB-COF was linked to structural deficiencies: missing in-plane polarization units, diminished dipole moments, and absence of the electron-deficient BT unit, respectively. These results underscore that structural factors (polarization motifs, dipole optimization, and BT integration) directly determine efficiency by regulating charge separation and polarization dynamics. These findings not only unravel the structure-property relationships in piezoelectric COFs but also provide a molecular blueprint for the design of multifunctional catalytic materials that harness mechanical-optical energy conversion.

## Methods

### Materials

All chemicals and reagents were of analytical grade and were used as received. The 1,2-dichlorobenzene (o-DCB, 99%), anhydrous n-butanol (99.4%), dioxane (99%), mesitylene (99%), and pyrrolidine (Py, 98%) were sourced from Macklin Chemicals. 2,4,6-tris(4-aminophenyl)triazine (TP), 97%, 4,4'-diamino-substituted p-terphenyl (SB, >97.0%), 4,4'-(benzo-2,1,3-thiadiazole-4,7-diyl)dianiline (BT-OF, 98%), and benzene-1,3,5-tricarbaldehyde (BTA, >98.0%) were obtained from Jilin Chinese Academy of Sciences-Yanshen Technology Co. Ltd.

### Characterization

PXRD patterns were collected on a PANalytical Empyrean diffractometer using Cu K $\alpha$  radiation ( $\lambda = 1.54 \text{ \AA}$ ) operated at 45 kV and 35 mA. FT-IR spectra were acquired with a Thermo Fisher Nicolet Avatar 6700 FT-IR spectrometer. UV-Vis absorption spectra were recorded on a Shimadzu UV-2700 spectrophotometer. Nitrogen sorption isotherms were measured at 77 K using an iPore400 analyzer. Prior to measurement, samples were degassed at 120 °C under dynamic vacuum ( $<10^{-3}$  Torr) for 10 h. Specific surface areas were determined using the BET method, and pore size distributions were derived from the sorption isotherms via NLDFT. XPS was performed on a VG ESCALAB250 system. TEM was carried out on a JEOL JEM-2010 instrument. The piezoelectric response was characterized by PFM using a Bruker Dimension Icon atomic force microscope. Photo-enhanced KPFM measurements were conducted using an AFM system equipped with an SKPM module and a xenon lamp source.

### Piezo-photocatalytic H<sub>2</sub> and H<sub>2</sub>O<sub>2</sub> evolution

The photocatalytic reaction was conducted in a 40 mL cylindrical optical reactor (outer diameter: 27.5 mm, height: 95 mm) containing 2 mg of catalyst dispersed in 20 mL of ultrapure water. The suspension was simultaneously irradiated with a 300 W Xe lamp (CEL-PF300-T9,

Beijing Zhongjiao Jinyuan) and ultrasonicated (JP10IT cleaner, 40 kHz, 60 W; Shenzhen Jiemen). The lamp was equipped with a visible light cut-off filter ( $\lambda \geq 420$  nm) to provide an incident light intensity of  $1000 \text{ W m}^{-2}$ , as calibrated by a solar power meter (Model SM206-SOLAR). The reaction temperature was maintained at  $20.0 \pm 0.5$  °C by a circulating cooling water system.

Prior to reaction, the system was purged by three alternating cycles of evacuation and argon purging (each 5 min) to ensure an anaerobic environment. During the reaction, 100  $\mu\text{L}$  of headspace gas was periodically extracted with a gas-tight syringe for hydrogen analysis by gas chromatography (GC, FULI GC9790 PLF-01, FULI instruments) equipped with a thermal conductivity detector (TCD). The  $\text{H}_2$  yield was determined using a standard calibration curve (Fig. S69A).

The concentration of hydrogen peroxide ( $\text{H}_2\text{O}_2$ ) was quantified via an enzymatic method using horseradish peroxidase (HRP) to catalyze the reaction between  $\text{H}_2\text{O}_2$  and 3,3',5,5'-tetramethylbenzidine (TMB).

The piezo-photocatalytic production of  $\text{H}_2$  and  $\text{H}_2\text{O}_2$  was investigated under varying ultrasonic intensities and frequencies. The experiments employed a multi-frequency ultrasonic cleaner (YNLH0203-204060, Shenzhen Yunyi) with selectable frequencies (20, 40, 60 kHz) and corresponding powers (30, 60, 120 W). All other conditions were consistent with those described above.

### Measurement of $\text{H}_2\text{O}_2$

The  $\text{H}_2\text{O}_2$  concentration was quantified using a 3,3',5,5'-tetramethylbenzidine (TMB)-based enzymatic assay, in which horseradish peroxidase (HRP) catalyzes the oxidation of TMB by  $\text{H}_2\text{O}_2$ .

The TMB stock solution was prepared by first dissolving 15 mg of TMB in 0.3 mL of dimethylsulfoxide (DMSO). This solution was then mixed with 5 mL of glycerol and 45 mL of an aqueous solution containing 20 mg of ethylenediaminetetraacetic acid (EDTA) and 95 mg of citric acid. The mixture was finally diluted to a total volume of 500 mL with deionized water. The HRP solution was prepared by dissolving 2 mg of the enzyme in 10 mL of deionized water.

For the calibration, 200  $\mu\text{L}$  of the TMB solution and 10  $\mu\text{L}$  of the HRP solution were added to a known concentration of  $\text{H}_2\text{O}_2$  (100  $\mu\text{L}$ ). After 3 min of reaction, HCl (10  $\mu\text{L}$ , 12 M) was added to stop the reaction, and the absorbance at 450 nm was measured by UV-Vis spectroscopy. A linear standard curve was established from these measurements and used to determine the  $\text{H}_2\text{O}_2$  concentration in the experimental samples. The testing method for the actual samples was identical to that used for the reference standard. The  $\text{H}_2\text{O}_2$  yield was calculated based on these calibration curves (Fig. S69B, C).

### Apparent quantum yields (AQYs) measurements

Apparent quantum yields (AQYs) were determined using 5 mg of samples dispersed in 20 mL of water, with a 300 W Xe lamp (CEL-PF300-T9, Beijing Zhongjiao Jinyuan Technology Co., Ltd.) equipped with band-pass filters ( $\lambda = 450, 500, 550, 600$  and  $650$  nm) as the incident light source (irradiation area:  $0.25 \text{ cm}^2$ ), under the combined conditions of irradiation and ultrasonic assistance for 30 min. The light intensity was measured with a solar power meter (Model SM206-SOLAR). The AQY was calculated using the following formula (1):

$$\eta = \frac{2 \times M \times N_A \times h \times c}{S \times P \times t \times \lambda} \times 100\% \quad (1)$$

Where  $M$  is the amount of  $\text{H}_2$  produced (mol),  $N_A$  is the Avogadro constant ( $6.022 \times 10^{23}/\text{mol}$ ),  $h$  is the Planck constant ( $6.626 \times 10^{-34}$  J s),  $c$  is the speed of light ( $3 \times 10^8$  m/s),  $S$  is the irradiation area of the incident light ( $\text{m}^2$ ),  $P$  is the intensity of the incident light ( $\text{W}/\text{m}^2$ ),  $t$  is the photoreaction time (s), and  $\lambda$  is the wavelength of the monochromatic light (m).

By substituting the known constants, we obtained the following simplified formula (2) for the AQY:

$$\eta = \frac{2 \times M \times 2.66 \times 10^9}{P \times \lambda} \times 100\% \quad (2)$$

Where  $M$  is the amount of  $\text{H}_2$  produced (mol),  $P$  is the intensity of the incident light ( $\text{W}/\text{m}^2$ ), and  $\lambda$  is the wavelength of the monochromatic light (nm). Specific values are provided in Table S14.

### Trapping experiments of hydroxyl radicals

An aqueous terephthalic acid (TA) solution (40 mL, 0.5 mM) was formulated in a 2 mM NaOH medium and then transferred into a quartz reactor. A 5 mg portion of the photocatalyst was uniformly dispersed in the aforementioned solution. The resulting mixture was exposed to visible light irradiation (300 W Xe lamp,  $\lambda > 420$  nm, light intensity:  $1000 \text{ W}/\text{m}^2$ ) for 1 h at 20 °C under constant magnetic stirring. Following the irradiation process, the suspension was subjected to centrifugation at 10,000 rpm for 10 min. The fluorescence emission intensity of the supernatant was determined at 425 nm (excitation wavelength: 315 nm) via a fluorescence spectrometer.

### Piezo-photoelectrochemical measurements

Piezo-photoelectrochemical measurements were performed using a standard three-electrode setup on a CHI660E electrochemical workstation, under visible light ( $\lambda \geq 420$  nm) and ultrasonic irradiation. The working electrode was prepared by dispersing 2 mg of catalyst in a mixture of 0.5 mL ethanol and 10  $\mu\text{L}$  Nafion solution, followed by sonication for 5 min to obtain a homogeneous suspension. Next, 50  $\mu\text{L}$  of the suspension was drop-cast onto a pre-cleaned ITO glass substrate ( $0.5 \times 0.5 \text{ cm}^2$ ) fixed with double-sided tape. A proton exchange membrane ( $1 \times 1 \text{ cm}^2$ ) was then placed on the catalyst-coated region and hot-pressed at 100 °C under 350 psi pressure for 3 min, thereby forming the working electrode (Fig. S70).

Mott-Schottky analysis was carried out using a three-electrode configuration, where the COF/ITO glass served as the working electrode, a platinum (Pt) plate functioned as the counter electrode, and a saturated Ag/AgCl electrode acted as the reference. The electrolyte consisted of 30 mL deionized water with 0.20 M  $\text{Na}_2\text{SO}_4$ . This study involved applying a polarization potential from  $-1.2$  to  $1.6$  V (vs. SCE), with alternating potential frequencies of 500, 1000, and 1500 Hz employed throughout the study.

Photocurrent tests were conducted under the conditions of irradiation, sonication, or their simultaneous application. EIS tests were conducted at a bias voltage of  $-0.4$  V, covering irradiation, sonication, or their combined action, with a frequency range of 0.001–100000 Hz. For EIS tests performed under ultrasound, the electrochemical cell was secured in an ultrasonic bath. The acquired EIS data were fitted with a suitable equivalent circuit<sup>17</sup>.

### In situ high-pressure PL, IR, and UV-Vis absorption measurements

High-pressure experiments utilized a symmetric diamond anvil cell (DAC) (Fig. S71) equipped with ultra-low fluorescence diamond anvils (culet diameter: 400  $\mu\text{m}$ ). Samples were loaded into a 150  $\mu\text{m}$ -diameter chamber laser-drilled in a pre-indented T301 stainless steel gasket (thickness: 45  $\mu\text{m}$ ), with silicon oil (PL/UV-Vis) or KBr (IR) selected as pressure-transmitting media. The ruby fluorescence technique was utilized for pressure determination, relying on the spectral shift of the R1 line in ruby fluorescence. All the aforementioned measurements were performed at 298 K.

**Spectroscopic measurements.** Photoluminescence (PL): excited with a 355 nm semiconductor laser (with power stabilized to avoid intensity-related artifacts), and the corresponding spectra were collected by an Ocean Optics QE65000 fiber spectrometer (Fig. S72).

UV-Vis absorption: a deuterium-halogen excitation source was coupled to the same spectrometer, with a focus on excitonic absorption bands (Fig. S73).

Infrared (IR): recorded using a Nicolet iN10 microscope spectrometer (equipped with a liquid N<sub>2</sub>-cooled MCT detector), where KBr was used as the pressure-transmitting medium (Fig. S74).

### In situ EPR monitoring experiments

EPR spectra were recorded at 298 K using a Magnetech ESR 5000 spectrometer (X-band, 9.85 GHz) (Fig. S75) with the adoption of the following instrumental parameters: modulation amplitude of 1.000 G, modulation frequency of 100 kHz, center field of 3500 G, and sweep width of 100 G. For in situ radical detection, 10 mg of the COF composite was dispersed in 20 mL of an aqueous solution supplemented with 200  $\mu$ L of 0.1 M DMPO as the spin trap, and then exposed to simultaneous ultrasonic treatment (40 kHz, 60 W) and visible-light irradiation (300 W Xe lamp,  $\lambda \geq 420$  nm) in a 40 mL quartz reactor. The resulting reaction mixture was continuously circulated through the EPR sample cell by a peristaltic pump at a flow rate of 6 mL/min, facilitating real-time detection at 30-s intervals.

### High piezoelectric coefficient ( $d_{33}$ ) test

The powder sample was subjected to a pressure of 4 tons for tableting to prepare a flake-shaped specimen, which was then placed in an oil bath for polarization treatment. The polarization conditions were as follows: the polarization voltage was 1400 V, the leakage current was controlled at 0.05 mA, the polarization temperature was room temperature, and the polarization duration was set to 0.5 h. The test sample was further tested between the upper and lower probes. The electromagnetic drive part in the test head generated a low-frequency alternating force of approximately 0.25 N at a frequency of 110 Hz. The two piezoelectric signals generated by the positive piezoelectric effect were then processed by the instrument, which displayed the  $d$  value.

### Calculation method

All DFT calculations in this work were calculated with the Vienna ab initio simulation package (VASP, version 6.3.0), implemented with plane waves and the projector augmented wave method. The Perdew-Burke-Ernzerhof (PBE) functionals were coupled with van der Waals (vdW) dispersion corrections of the zero-damping DFT-D3 method of Grimme<sup>51,52</sup>. All structures of these COFs (see Supplementary Data 1–4) were optimized until all Hellmann-Feynman forces on atoms were less than 0.005 eV/Å with cell optimization and an energy cutoff of 550 eV and a  $\Gamma$ -centered  $k$ -mesh with a  $k$ -point distance of  $<2\pi/36$  Å<sup>-1</sup>. The piezoelectric tensors, effective Born charges of these COFs were determined from the response to finite electric fields ( $E = 0.001$  eV/Å). Geometry optimizations and electronic structure characterizations of the molecules were performed at the B3LYP/6-311G level using the Gaussian 16<sup>53</sup>. Our DFT calculations employed idealized COF models, which cannot fully capture the inherent structural complexity and dynamic nature of the real systems.

### Synthesis experiments

**Synthesis of 4,4'-(5,6-difluorobenzo[c][1,2,5]thiadiazole-4,7-diyl)dianiline (BT-1F).** The reaction was conducted in a mixture of toluene (45 mL), ethanol (12 mL), and water (9 mL) containing 4,7-dibromo-5-fluoro-2,1,3-benzothiadiazole (0.80 g, 2.55 mmol), 4-(4,4,5,5-tetramethyl-1,3,2-dioxaborolan-2-yl)aniline (1.34 g, 6.12 mmol), and K<sub>2</sub>CO<sub>3</sub> (2.90 g, 27.30 mmol). Under an argon atmosphere, established by 30 min of purging, Pd(PPh<sub>3</sub>)<sub>4</sub> (0.29 g, 0.25 mmol) was added to initiate the Suzuki coupling. The reaction proceeded at 100 °C over 24 h. Standard workup included cooling, dilution with dichloromethane (20 mL), and removal of the catalyst by filtration through a Celite pad. The crude product obtained after solvent evaporation was subjected to column chromatography, yielding the desired compound as an

orange solid (617.0 mg) with a yield of 72%. <sup>1</sup>H NMR (400 MHz, DMSO-*d*<sub>6</sub>)  $\delta$  (ppm) 7.85 (d,  $J = 8.6$  Hz, 2H), 7.73 (d,  $J = 12.5$  Hz, 1H), 7.48 (d,  $J = 8.5$ , 1.6 Hz, 2H), 6.81–6.62 (m, 4H), 5.52 (s, 2H), 5.41 (s, 2H).

**Synthesis of 4,4'-(5,6-difluorobenzo[c][1,2,5]thiadiazole-4,7-diyl)dianiline (BT-2F)**<sup>28</sup>. The reaction was conducted in a mixture of toluene (45 mL), ethanol (12 mL), and water (9 mL) containing 4,7-dibromo-5-fluoro-2,1,3-benzothiadiazole (0.84 g, 2.55 mmol), 4-(4,4,5,5-tetramethyl-1,3,2-dioxaborolan-2-yl)aniline (1.34 g, 6.12 mmol), and K<sub>2</sub>CO<sub>3</sub> (2.90 g, 27.30 mmol). Under an argon atmosphere, established by 30 min of purging, Pd(PPh<sub>3</sub>)<sub>4</sub> (0.29 g, 0.25 mmol) was added to initiate the Suzuki coupling. The reaction proceeded at 100 °C over 24 h. Standard workup included cooling, dilution with dichloromethane (20 mL), and removal of the catalyst by filtration through a Celite pad. The crude product obtained after solvent evaporation was subjected to column chromatography, yielding the desired compound as an orange solid (722.0 mg) with a yield of 80%. <sup>1</sup>H NMR (400 MHz, CDCl<sub>3</sub>)  $\delta$  (ppm) = 7.62 (d,  $J = 8.8$  Hz, 4H), 6.83 (d,  $J = 8.8$  Hz, 4H), 3.94 (s, 4H).

**Synthesis of TP-BT-OF-COF**<sup>54</sup>. 2,4,6-Trihydroxybenzene-1,3,5-tricarbaldehyde (TP) (10.5 mg, 0.05 mmol), 4,4'-(benzo-2,1,3-thiadiazole-4,7-diyl)dianiline (BT-OF) (23.9 mg, 0.08 mmol), *o*-1,2-dichlorobenzene (0.75 mL), *n*-butanol (0.25 mL), and Py (0.10 mL) were combined in a Pyrex tube. After 10 min of sonication for homogenization, the mixture was flash-frozen in liquid nitrogen (77 K) and subjected to three freeze-pump-thaw cycles. The tube was then evacuated to 100 mTorr, sealed, and heated at 120 °C for 3 days. The brown precipitate that formed was collected via centrifugation and washed sequentially with tetrahydrofuran and anhydrous acetone. The resulting powder was activated by stirring in dimethylsulfoxide for 6 h. Subsequent washing with tetrahydrofuran and drying at 60 °C afforded a crimson powder (26 mg, 75% yield).

**Synthesis of TP-BT-1F-COF.** 2,4,6-Trihydroxybenzene-1,3,5-tricarbaldehyde (TP) (10.5 mg, 0.05 mmol), 4,4'-(5-difluorobenzo[c][1,2,5]thiadiazole-4,7-diyl)dianiline (BT-1F) (25.3 mg, 0.08 mmol), *o*-1,2-dichlorobenzene (0.75 mL), *n*-butanol (0.25 mL), and Py (0.10 mL) were combined in a Pyrex tube. After 10 min of sonication for homogenization, the mixture was flash-frozen in liquid nitrogen (77 K) and subjected to three freeze-pump-thaw cycles. The tube was then evacuated to 100 mTorr, sealed, and heated at 120 °C for 3 days. The brown precipitate that formed was collected via centrifugation and washed sequentially with tetrahydrofuran and anhydrous acetone. The resulting powder was activated by stirring in dimethylsulfoxide for 6 h. Subsequent washing with tetrahydrofuran and drying at 60 °C afforded an orange powder (28 mg, 80% yield).

**Synthesis of TP-BT-2F-COF.** 2,4,6-Trihydroxybenzene-1,3,5-tricarbaldehyde (TP) (10.5 mg, 0.05 mmol), 4,4'-(5,6-difluorobenzo[c][1,2,5]thiadiazole-4,7-diyl)dianiline (BT-2F) (26.5 mg, 0.08 mmol), *o*-1,2-dichlorobenzene (0.75 mL), *n*-butanol (0.25 mL), and Py (0.10 mL) were combined in a Pyrex tube. After 10 min of sonication for homogenization, the mixture was flash-frozen in liquid nitrogen (77 K) and subjected to three freeze-pump-thaw cycles. The tube was then evacuated to 100 mTorr, sealed, and heated at 120 °C for 3 days. The brown precipitate that formed was collected via centrifugation and washed sequentially with tetrahydrofuran and anhydrous acetone. The resulting powder was activated by stirring in dimethylsulfoxide for 6 h. Subsequent washing with tetrahydrofuran and drying at 60 °C afforded an orange powder (30 mg, 80% yield).

**Synthesis of SB-COF.** 2,4,6-Trihydroxybenzene-1,3,5-tricarbaldehyde (TP) (16.8 mg, 0.08 mmol), 4,4'-diamino-substituted *p*-terphenyl (SB) (32.1 mg, 0.12 mmol), dioxane (0.67 mL), mesitylene (0.33 mL), and Py (0.10 mL) were mixed in a Pyrex tube. After 10 min of sonication for

homogenization, the mixture was flash-frozen in liquid nitrogen (77 K) and subjected to three freeze-pump-thaw cycles. The tube was then evacuated to 100 mTorr, sealed, and heated at 120 °C for 3 days. The brown precipitate that formed was collected via centrifugation and washed sequentially with tetrahydrofuran and anhydrous acetone. The resulting powder was activated by stirring in dimethylsulfoxide for 6 h. Subsequent washing with tetrahydrofuran and drying at 60 °C afforded a deep yellow powder (40 mg, 80% yield).

**Synthesis of the BTA-BT-OF-COF<sup>29</sup>.** A mixture containing benzene-1,3,5-tricarbaldehyde (BTA, 8.1 mg, 0.05 mmol) and 4,4'-(benzo-2,1,3-thiadiazole-4,7-diyl)dianiline (BT-OF) (24 mg, 0.08 mmol) in *o*-dichlorobenzene/mesitylene/aqueous acetic acid (6 M) (0.50: 0.50: 0.30 mL) was sonicated for 10 min to achieve a homogeneous solution. The mixture was flash-frozen in liquid nitrogen (77 K) and subjected to three freeze-pump-thaw cycles. The tube was then evacuated to 100 mTorr, sealed, and heated at 120 °C for 3 days. The brown precipitate that formed was collected via centrifugation and washed sequentially with tetrahydrofuran and anhydrous acetone. The resulting powder was activated by stirring in dimethylsulfoxide for 6 h. Subsequent washing with tetrahydrofuran and drying at 60 °C afforded a yellow powder (22 mg, 70%).

## Data availability

The data supporting the findings of this study are available within the paper and its Supplementary Information/Source data files. Source data are provided in this paper.

## References

- Luan, B. B. et al. Construction of COF/COF organic S-scheme heterostructure for enhanced overall water splitting. *Adv. Mater.* **36**, 2412653 (2024).
- Wang, X. et al. Sulfone-containing covalent organic frameworks for photocatalytic hydrogen evolution from water. *Nat. Chem.* **10**, 1180–1189 (2018).
- Li, X. A. et al. A Z-scheme photosensitive MOC/g-C<sub>3</sub>N<sub>4</sub> composite catalyst for efficient visible-light driven half and overall water splitting. *J. Mater. Chem. A* **12**, 32307–32317 (2024).
- Li, X. A. et al. A direct Z-scheme quasi-2D/2D heterojunction constructed by loading photosensitive metal-organic nanorings with Pd single atoms on graphitic-C<sub>3</sub>N<sub>4</sub> for superior visible light-driven H<sub>2</sub> production. *Sol. RRL* **7**, 2300148 (2023).
- Liu, P. et al. Recent advances in the utilization of chiral covalent organic frameworks for asymmetric photocatalysis. *Molecules* **29**, 5006 (2024).
- Hong, K. S. et al. Direct water splitting through vibrating piezoelectric microfibers in water. *J. Phys. Chem. Lett.* **1**, 997–1002 (2010).
- Huang, H. W. et al. Macroscopic polarization enhancement promoting photo- and piezoelectric-induced charge separation and molecular oxygen activation. *Angew. Chem. Int. Ed.* **56**, 11860–11864 (2017).
- You, H. L. et al. Piezoelectrically/pyroelectrically-driven vibration/cold-hot energy harvesting for mechano-/pyro-bi-catalytic dye decomposition of NaNbO nanofibers. *Nano Energy* **52**, 351–359 (2018).
- Anh, N. H. et al. Unraveling precise locations of indium atoms in g-C<sub>3</sub>N<sub>4</sub> for ameliorating hydrogen peroxide piezo-photogeneration. *Sol. RRL* **8**, 2400034 (2024).
- Hu, C. et al. Exceptional cocatalyst-free photo-enhanced piezocatalytic hydrogen evolution of carbon nitride nanosheets from strong in-plane polarization. *Adv. Mater.* **33**, 2101751 (2021).
- Xu, M.-L. et al. Piezo-photocatalytic synergy in BiFeO<sub>3</sub>@COF Z-scheme heterostructures for high-efficiency overall water splitting. *Angew. Chem. Int. Ed.* **61**, e202210700 (2022).
- Wang, K. et al. The mechanism of piezocatalysis: energy band theory or screening charge effect?. *Angew. Chem. Int. Ed.* **61**, e202110429 (2022).
- Amdouni, W. et al. BiFeO<sub>3</sub> nanoparticles: the “Holy-Grail” of piezophotocatalysts?. *Adv. Mater.* **35**, 2301841 (2023).
- Su, R. et al. Strain-engineered nano-ferroelectrics for high-efficiency piezocatalytic overall water splitting. *Angew. Chem. Int. Ed.* **60**, 16019–16026 (2021).
- Shu, A. et al. Electric effects reinforce charge carrier behaviour for photocatalysis. *Energy Environ. Sci.* **17**, 4907–4928 (2024).
- Hu, H. et al. Dual modification of metal-organic frameworks for exceptional high piezo-photocatalytic hydrogen production. *Adv. Mater.* **37**, 2419023 (2025).
- Zhang, C. et al. Piezo-photocatalysis over metal-organic frameworks: promoting photocatalytic activity by piezoelectric effect. *Adv. Mater.* **33**, 2106308 (2021).
- Chen, J.-P. et al. Piezocatalytic performances of conjugated microporous polymers with donor-acceptor structures for overall water splitting. *ACS Catal.* **14**, 7853–7866 (2024).
- Chen, C. et al. Spatially separated redox centers in anthraquinone-grafted metal-organic frameworks for efficient piezo-photocatalytic H<sub>2</sub>O<sub>2</sub> production. *Angew. Chem. Int. Ed.* **64**, e202425656 (2025).
- Ghosh, S. et al. Identification of prime factors to maximize the photocatalytic hydrogen evolution of covalent organic frameworks. *J. Am. Chem. Soc.* **142**, 9752–9762 (2020).
- Liu, N. et al. Dual-acceptor engineering in pyrene-based covalent organic frameworks for boosting photocatalytic hydrogen evolution. *Adv. Energy Mater.* **14**, 2402395 (2024).
- Lin, Z. et al. Controlling crystallization in covalent organic frameworks to facilitate photocatalytic hydrogen production. *Nat. Commun.* **16**, 1940 (2025).
- Wang, Y. X. et al. Boosting multicolor emission enhancement in two-dimensional covalent-organic frameworks via the pressure-tuned π-π stacking mode. *Nano Lett.* **25**, 2141–2149 (2025).
- Fang, J. et al. Piezofluorochromism in covalent organic frameworks: pressure-induced emission enhancement and blue-shifted emission. *Angew. Chem. Int. Ed.* **63**, e202409099 (2024).
- Gu, Q. F. et al. High-performance piezoelectric two-dimensional covalent organic frameworks. *Angew. Chem. Int. Ed.* **63**, e202409708 (2024).
- Li, Z. et al. Covalent organic frameworks for boosting H<sub>2</sub>O<sub>2</sub> photosynthesis via the synergy of multiple charge transfer channels and polarized field. *Angew. Chem. Int. Ed.* **64**, e202420218 (2025).
- Liang, Z. Z. et al. A direct Z-scheme single-atom MOC/COF piezophotocatalytic system for overall water splitting. *ACS Catal.* **14**, 10447–10461 (2024).
- Chen, W. et al. Modulating benzothiadiazole-based covalent organic frameworks via halogenation for enhanced photocatalytic water splitting. *Angew. Chem. Int. Ed.* **59**, 16902–16909 (2020).
- Wang, J. et al. Integrating dual-metal sites into covalent organic frameworks for enhanced photocatalytic CO<sub>2</sub> reduction. *ACS Catal.* **13**, 4316–4329 (2023).
- Zhao, Z. et al. Fabrication of robust covalent organic frameworks for enhanced visible-light-driven H<sub>2</sub> evolution. *ACS Catal.* **11**, 2098–2107 (2021).
- Gruverman, A. et al. Piezoresponse force microscopy and nanoferroic phenomena. *Nat. Commun.* **10**, 1661 (2019).
- Li, Z. et al. Dipole field in nitrogen-enriched carbon nitride with external forces to boost the artificial photosynthesis of hydrogen peroxide. *Nat. Commun.* **14**, 5742 (2023).
- Guan, L. et al. Bottom-up synthesis of piezoelectric covalent triazine-based nanotube for hydrogen peroxide production from water and air. *Angew. Chem. Int. Ed.* **64**, e202419867 (2025).

34. Ghosh, A. et al. Ferrielectric dipolar ordering in a donor-acceptor based covalent-organic framework for piezocatalytic water splitting. *Adv. Funct. Mater.* **35**, 2502787 (2025).
35. Wang, Y. X. et al. Pressure effects on metal/covalent-organic frameworks: structural and optical properties. *Sci. China Chem.* **67**, 2890–2903 (2024).
36. Wang, Y. X. et al. Tuning the photocatalytic activity through linkages of porous conjugated polymers based on triazines for a selective oxidation reaction. *Adv. Energy Sustain. Res.* **4**, 2200129 (2023).
37. Wu, M. et al. Pressure-induced restricting intermolecular vibration of a herringbone dimer for significantly enhanced multicolor emission in rotor-free truxene crystals. *J. Phys. Chem. Lett.* **13**, 2493–2499 (2022).
38. Wu, W. Z. et al. Piezotronics and piezo-phototronics for adaptive electronics and optoelectronics. *Nat. Rev. Mater.* **1**, 16031 (2016).
39. Sun, J. et al. Pyrene-based covalent organic frameworks for photocatalytic hydrogen peroxide production. *Angew. Chem. Int. Ed.* **62**, e202216719 (2023).
40. Chakraborty, A. et al. Enhancing photocatalytic hydrogen peroxide generation by tuning hydrazone linkage density in covalent organic frameworks. *Nat. Commun.* **16**, 503 (2025).
41. Wang, H. et al. A crystalline partially fluorinated triazine covalent organic framework for efficient photosynthesis of hydrogen peroxide. *Angew. Chem. Int. Ed.* **61**, e202202328 (2022).
42. Ma, J. et al. H<sub>2</sub>O<sub>2</sub> photosynthesis from H<sub>2</sub>O and O<sub>2</sub> under weak light by carbon nitrides with the piezoelectric effect. *J. Am. Chem. Soc.* **146**, 21147–21159 (2024).
43. Ma, Y. et al. Bifunctional RbBiNb<sub>2</sub>O<sub>7</sub>/poly(tetrafluoroethylene) for high-efficiency piezocatalytic hydrogen and hydrogen peroxide production from pure water. *Chem. Eng. J.* **446**, 136958 (2022).
44. Wen, N. et al. Dynamic bromine vacancy-mediated photocatalytic three-step three-electron oxygen reduction to hydroxyl radicals. *ACS Catal.* **14**, 11153–11163 (2024).
45. Han, J. et al. Comparative study on properties, structural changes, and isomerization of cis/trans-stilbene under high pressure. *J. Phys. Chem. C* **126**, 16859–16866 (2022).
46. Wang, X. L. et al. Dye-sensitized photoelectrochemical cells constructed using metal-free perylene diimide-based oxygen production polymers and calixarene dyes. *J. Mater. Chem. A* **12**, 22101–22111 (2024).
47. Wang, X.-L. et al. Polymer networks assembled by ruthenium catalysts for enhanced water splitting performance in calixarene dye-sensitized photoelectrochemical cells. *ChemSusChem* **18**, e202402395 (2024).
48. Zhang, J. et al. Enhancing photocatalytic performance of covalent organic frameworks via ionic polarization. *Nat. Commun.* **15**, 9576 (2024).
49. Qi, J.-X. et al. Ocean wave-driven covalent organic framework/ZnO heterostructure composites for piezocatalytic uranium extraction from seawater. *Nat. Commun.* **16**, 1078 (2025).
50. Zhou, Y. et al. The role of Fe species on NiOOH in oxygen evolution reactions. *ACS Catal.* **10**, 6254–6261 (2020).
51. Perdew, J. P. et al. Generalized Gradient Approximation Made Simple [Phys. Rev. Lett. **77**, 3865 (1996)]. *Phys. Rev. Lett.* **78**, 1396–1396 (1997).
52. Grimme, S. et al. A consistent and accurate ab initio parametrization of density functional dispersion correction (DFT-D) for the 94 elements H-Pu. *J. Chem. Phys.* **132**, 154104 (2010).
53. Lu, T. et al. Shermo: a general code for calculating molecular thermochemistry properties. *Comput. Theor. Chem.* **1200**, 113249 (2021).
54. Zhou, T. et al. PEG-stabilized coaxial stacking of two-dimensional covalent organic frameworks for enhanced photocatalytic hydrogen evolution. *Nat. Commun.* **12**, 3934 (2021).

## Acknowledgements

The authors gratefully acknowledge the financial support from the National Natural Science Foundation Project of China (grant No. 21975291 and 22275214), the NSF of Guangdong Province (grant No. 2022A1515011949 and 2024A1515012076), and “Climbing Program” Special Funds for the Cultivation of Guangdong College Students’ Scientific and Technological Innovation (grant No. pdjh2024b014). The authors thank Li Gong (Instrumental Analysis and Research Center, Sun Yat-sen University) for assistance with PFM and KPFM measurements. The authors thank Dr. Jingying Sun (Instrumental Analysis and Research Center, Sun Yat-sen University) for assistance with TEM measurements. The in situ high-pressure spectral experiments were performed at the B2 station, Synergetic Extreme Condition User Facility (SECUF).

## Author contributions

J.-M. Liu led the project, supervised the experimental work, and revised the paper. Z.-Z. Liang synthesized and characterized the COF samples, performed experiments and data analysis, and wrote the paper. Y. Wang, X.-A. Li, and X.-B. Peng performed experiments and interpreted the results. Y. Zhou and L.-M. Xiao conducted the structural simulations and DFT calculations and revised the paper. X. Yang and B. Zou conducted the pressure-dependent experiments and revised the paper. L. Gong conducted the KPFM and PFM experiments and revised the paper. All authors have read and commented on the paper.

## Competing interests

The authors declare no competing interests.

## Additional information

**Supplementary information** The online version contains supplementary material available at <https://doi.org/10.1038/s41467-025-67467-0>.

**Correspondence** and requests for materials should be addressed to Xinyi Yang, Yecheng Zhou or Jun-Min Liu.

**Peer review information** *Nature Communications* thanks the anonymous reviewer(s) for their contribution to the peer review of this work. A peer review file is available.

**Reprints and permissions information** is available at <http://www.nature.com/reprints>

**Publisher’s note** Springer Nature remains neutral with regard to jurisdictional claims in published maps and institutional affiliations.

**Open Access** This article is licensed under a Creative Commons Attribution-NonCommercial-NoDerivatives 4.0 International License, which permits any non-commercial use, sharing, distribution and reproduction in any medium or format, as long as you give appropriate credit to the original author(s) and the source, provide a link to the Creative Commons licence, and indicate if you modified the licensed material. You do not have permission under this licence to share adapted material derived from this article or parts of it. The images or other third party material in this article are included in the article’s Creative Commons licence, unless indicated otherwise in a credit line to the material. If material is not included in the article’s Creative Commons licence and your intended use is not permitted by statutory regulation or exceeds the permitted use, you will need to obtain permission directly from the copyright holder. To view a copy of this licence, visit <http://creativecommons.org/licenses/by-nc-nd/4.0/>.

© The Author(s) 2025, modified publication 2026